JOURNAL OF
PETROLOGY

Journal of Petrology, 2019, Vol. 60, No. 1, 151–176
doi: 10.1093/petrology/egy109
Advance Access Publication Date: 5 December 2018
Original Article

OXFORD

Allanite Petrochronology in Fresh and Retrogressed Garnet–Biotite Metapelites from the Longmen Shan (Eastern Tibet)

Laura Airaghi [1]*, Emilie Janots[1], Pierre Lanari [2], Julia de Sigoyer[1] and Valérie Magnin[1]

[1]ISTerre, Université Grenoble Alpes, Université Savoie Mont Blanc, CNRS, IRD, IFSTTAR, Grenoble, France; [2]Institute of Geological Sciences, University of Bern, CH-3012 Bern, Switzerland

*Corresponding author. Present address: ISTeP, Sorbonne Université, 4 Place Jussieu, 75005 Paris, France. E-mail: laura.airaghi@upmc.fr

Received September 12, 2017; Accepted November 19, 2018

ABSTRACT

Linking the timing of allanite growth to metamorphic conditions in metapelites is particularly challenging because of the large variety of allanite textures and chemical compositions. This study focuses on five garnet–biotite metapelites retrogressed to different extents, from the internal domain of the Longmen Shan (eastern Tibet) from which few petrochronological data documenting the metamorphic ages are available. Microstructural observations were combined with whole-rock compositions, detailed mineral characterization, phase equilibria modelling, and *in situ* U–Th/Pb allanite dating to gain insights into the allanite reactivity relative to other rock-forming minerals. All samples experienced similar peak temperatures of 560–600°C. Allanite is the main rare earth element (REE)-bearing accessory mineral but it exhibits different textures, such as epidote rims with distinct REE contents as well as late inclusion-like dissolution features. Garnet is, along with allanite, critical to reconstruct the REE budget of these rocks. In the two samples where allanite is observed as inclusions in garnet, garnet shows no textural zoning and a low Y content (<90 ppm). This is attributed to early Y fractionation in allanite and epidote rims with no further equilibration with garnet. This allanite is therefore pre-garnet ($T < 520$°C). In the sample where allanite is observed only in the matrix, both garnet and allanite–epidote rims exhibit more complex textural and compositional zoning, with a higher Y content in garnet. The Y incorporation in garnet is attributed to a series of reactions involving allanite, interpreted as syn- to post-garnet growth ($T > 520$°C). This relative chronology is confirmed by *in situ* U–Th/Pb allanite dating: pre-garnet allanite shows ages of *c.* 200 Ma, whereas syn- to post-garnet allanite has ages of *c.* 180 Ma. The timing of allanite appearance strongly correlates with the biotite-in reaction predicted by the models and observed in microstructures. In the two samples collected close to the major Wenchuan Shear Zone—deformed up to mylonitization and retrogressed under greenschist-facies conditions (3–4 ± 1 kbar, 350–400°C)—allanite still preserves the peak metamorphic ages (*c.* 200 and *c.* 180 Ma). Allanite and its epidote rims, however, are fragmented and partly replaced by a retrograde assemblage of Qz + Pb-depleted (<100 ppm) monazite, providing an age <90–100 Ma. Our results allow different metamorphic stages for the studied transect in the central Longmen Shan to be refined: a prograde path at *c.* 200 Ma, a thermal relaxation and exhumation from *c.* 180 Ma, and a late greenschist overprint. This study also shows that when allanite is the principal phase in a mineral assemblage datable by U–Th/Pb, detailed observations of allanite textures may be highly informative in constraining the timing of its growth relative to other major mineral phases.

Key words: allanite; amphibolite-facies metamorphism; greenschist-facies metamorphism; metapelites; compositional maps; U–Th/Pb dating

INTRODUCTION

The use of allanite [rare earth element (REE)-epidote of idealized structural formula $CaREEAl_2Fe^{2+}Si_3O_{11}O(OH)$; Gieré & Sorensen, 2004] as a geochronometer has progressively increased in recent decades to date metamorphic stages (Gregory *et al.*, 2007, 2012; Janots *et al.*, 2009; Kim *et al.*, 2009; Radulescu *et al.*, 2009; Cenki-Tok *et al.*, 2011; Rubatto *et al.*, 2011; Janots & Rubatto, 2014; Loury *et al.*, 2016; Giuntoli *et al.*, 2018). Allanite is stable over a wide range of temperature (T) and pressure (P) (Wing *et al.*, 2003; Janots *et al.*, 2006, 2008; Tomkins & Pattison, 2007), including relatively low-grade metamorphic conditions, where it may represent the only target mineral for U–Th/Pb dating (e.g. Janots *et al.*, 2009; Janots & Rubatto, 2014).

The metamorphic sequence of REE-bearing minerals in metapelites at low- to medium-grade metamorphism is relatively well known (see Engi, 2017, for a review). Petrological investigations show that allanite commonly forms at the expense of detrital or metamorphic monazite (or more rarely detrital allanite; Goswami-Banerjee & Robyr, 2015) at 400–450°C (Janots *et al.*, 2008, 2011), close to the biotite-in reaction (Wing *et al.*, 2003; Goswami-Banerjee & Robyr, 2015), and that it is consumed to form monazite at the staurolite-in reaction (e.g. Wing *et al.*, 2003; Corrie & Kohn, 2008; Janots *et al.*, 2008). Hence, in medium-grade garnet–biotite metapelites, allanite (± apatite and zircon) is likely to represent the main host for Th, U, REE (corresponding to lanthanides) and Y. In these rocks, allanite can exhibit a large variety of textures depending on the reaction history during metamorphism (Sorensen, 1991; Finger *et al.*, 1998; Janots *et al.*, 2008, 2011). Although efforts have been devoted to strengthen our understanding of the reaction mechanisms between allanite and monazite (Smith & Barreiro, 1990; Finger *et al.*, 1998, 2016; Janots *et al.*, 2008; Spear & Pyle, 2010; Regis *et al.*, 2012; Goswami-Banerjee & Robyr, 2015), less is known regarding the reactivity of allanite and the timing of allanite growth relative to other index metamorphic minerals (e.g. garnet and biotite), within the allanite stability field. This is, however, crucial to accurately link allanite ages to metamorphic stages (Engi, 2017).

The present study focuses on garnet–biotite metapelites from the central Longmen Shan, at the eastern border of the Tibetan plateau (Fig. 1a). The rocks underwent medium-grade metamorphism at amphibolite-facies conditions (Dirks *et al.*, 1994; Worley & Wilson, 1996; Airaghi *et al.*, 2017*b*) and were overprinted to different extents under greenschist-facies conditions (Airaghi *et al.*, 2017*a*). Detailed petrological investigations and $^{40}Ar/^{39}Ar$ biotite ages reveal a prograde to peak-P stage at *c.* 220–200 Ma and a peak-T at *c.* 180 Ma (Airaghi *et al.*, 2018*a*). The significance of Ar–Ar ages at 350–600°C is often controversial because of possible age resetting owing to Ar diffusion (e.g. Villa *et al.*, 2014; Cossette *et al.*, 2015; McDonald *et al.*, 2016). It is therefore crucial to test—in different locations—whether the successive P–T stages of the amphibolite-facies metamorphism are also recorded by geochronometers such as allanite, which can be dated by U–Th/Pb and have a high nominal closure temperature ($T > 700°C$; Rubatto *et al.*, 2001; Gregory *et al.*, 2012; Engi, 2017).

Five allanite-bearing metamorphic rocks, in which allanite exhibits a variety of complex microstructures, were selected for this study. To identify the timing and reaction processes responsible for allanite growth and resorption relative to other minerals, we combined microstructural observations, characterization of major minerals and allanite (and monazite when present) and thermobarometry with *in situ* U–Th/Pb allanite and monazite dating. This multi-method approach greatly improves our understanding of the metamorphic history of the medium-grade metapelites and, at the regional scale, allows the timing of metamorphism in the Longmen Shan to be more precisely constrained, with significant implications for the geodynamical history of eastern Tibet.

GEOLOGICAL SETTING

The Longmen Shan mountain belt is located at the eastern border of the Tibetan plateau, between the Songpan Ganze (SPG) block to the west and the Sichuan Basin (lying on the South China craton) to the east (Fig. 1a). Structural, petrological, geochronological and thermochronological studies provide several lines of evidence for three compressional phases that affected the belt in the past. The first one is linked to the Late Triassic–Early Jurassic closure of the Paleotethys (Chen & Wilson, 1995; Harrowfield & Wilson, 2005; Roger *et al.*, 2010; Yan *et al.*, 2011; Airaghi *et al.*, 2018*a*). The second one occurred during the Early Cretaceous (Airaghi *et al.*, 2017*b*, 2018*a*, 2018*b*) following the Lhasa–Qiangtang block collision. The third one is related to Cenozoic reactivation starting in the Eocene (Arne *et al.*, 1997; Kirby *et al.*, 2002; Richardson *et al.*, 2008; Godard *et al.*, 2009; Li *et al.*, 2012, 2015; Wang *et al.*, 2012).

From east to west three faults strike parallel to the belt: the Guanxian, Beichuan and the Wenchuan faults (GF, BF and WF in Fig. 1a). The WF is the Cenozoic expression of a Mesozoic tectonic discontinuity lying in a larger ductile fault zone, the Wenchuan Shear Zone (WSZ in Fig. 1b and c) subparallel to the WF. The Neoproterozoic South China Craton is exhumed in the Pengguan, Xuelongbao and Tonghua crystalline massifs, in the hanging wall of the major Beichuan and Wenchuan faults (Fig. 1a and b; Zhou *et al.*, 2006; Yan *et al.*, 2008). Crystalline massifs crop out through the metamorphosed Paleozoic to Mesozoic sedimentary cover.

Samples for this study were collected in the hanging wall of the Wenchuan fault, along a NW–SE cross-section between the Xuelongbao and Tonghua massifs (Fig. 1b), at a decreasing distance from the WF.

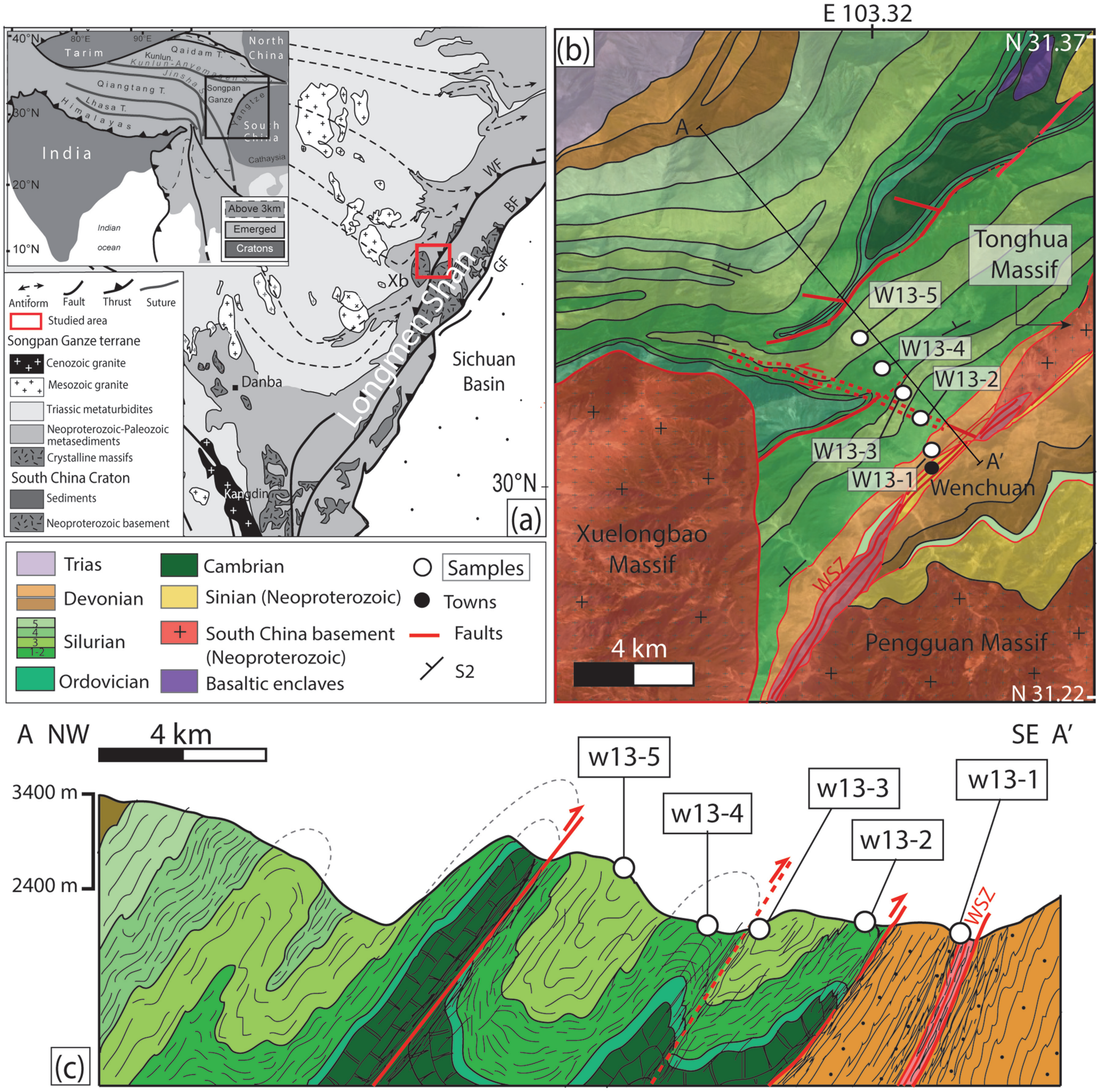

Fig. 1. (a) Simplified geological and structural map of the eastern border of the Tibetan plateau. The inset shows the location of the Longmen Shan area (black frame) at the India–Asia scale. GF, Guanxian fault; BF, Beichuan fault; WF, Wenchuan fault; Xb, Xuelongbao. Red frame indicates the location of the study area. (b) Detailed geological map of the study area. The ancient faults observed in the field are indicated in red. WSZ, Wenchuan Shear zone. The WF (within the WSZ) is the only tectonic discontinuity that is active at the present day. Sample locations are indicated by white dots. The red dashed fault represents the possible prolongation of the red continuous-line southern thrust in the Silurian sediments. (c) Cross-section along the profile AA′ in (b).

Here, sedimentary units include deformed and metamorphosed Silurian metapelites and metagreywackes (with minor limestones) folded in a tight system of SE-verging anticlines and synclines (Fig. 1c). East of the studied cross-section (AA′ in Fig. 1b) folds are oriented NE–SW; west of the studied cross-section they are oriented roughly east–west. A WNW–ESE-directed strike-slip fault is observed close to Wenchuan town (Fig. 1b). This fault may extend northwestward in a ductile shear zone, accommodating the transition between the domains characterized by the two different fold directions (Fig. 1b). The Cambrian–Ordovician units are thrusted over the Silurian metasediments along two NE–SW ancient thrusts (continuous red lines in Fig. 1b) on each side of the studied cross-section. Thrusts may vanish in the ductile strike-slip structure or may extend southward and northeastward in the Silurian sediments (Fig. 1b and c). The stratigraphic continuity along the cross-section, however, suggests that they would be related to an only minor vertical offset of the metasedimentary series (Fig. 1c).

PETROGRAPHY OF THE SAMPLES

Five samples were selected for this study (Fig. 2); their characteristics are summarized in Table 1. Samples w13-5, w13-4 and w13-3 are 'fresh' garnet–biotite metapelites consisting of Grt + Bt + Wm + Chl + Ilm + Qz

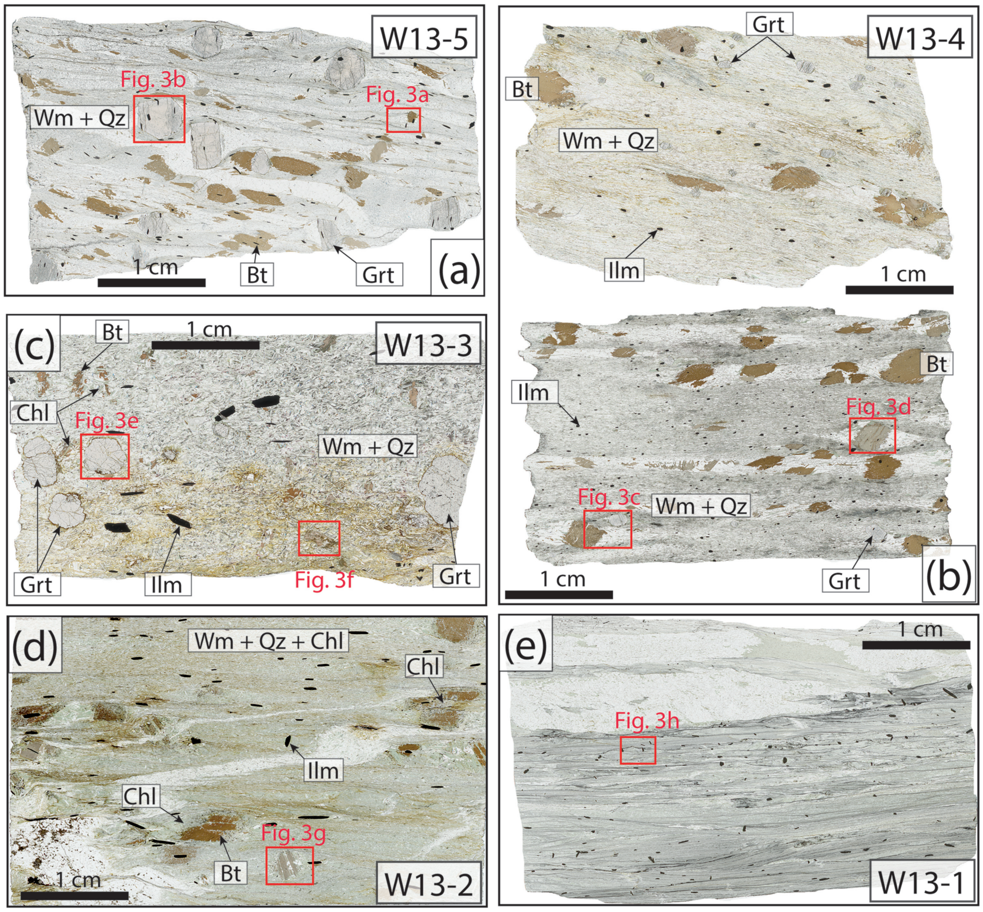

Fig. 2. Photographs of thin sections of the studied samples under plane-polarized light.

+Fs (mainly Ab) with Ap and Aln (± Mnz, ± Tur) as accessory phases [mineral abbreviations are from Whitney & Evans (2010) except for Wm = white mica]. Mineral proportions were obtained using the point counting method applying the software *JMicrovision* on a slide image of the thin section.

Samples w13-5 and w13-4 best preserve the cross-cutting and overprinting relations among successive microstructures. The main foliation is defined by S_2 cleavage domains (100–600 μm wide) made of elongated white mica grains (30–100 μm in size), quartz microlithons (Fig. 3a–d) and small biotite grains (200 μm in size) only in sample w13-5 (Fig. 3b). An earlier S_1 cleavage is preserved in asymmetric microfolds among the S_2 domains and is defined by 20–50 μm white mica (± chlorite) grains (e.g. Fig. 3a and c).

Metapelites w13-5 and w13-4 contain ~10 vol. % and ~8% of biotite, respectively, wrapped by the S_2 cleavage (Figs 2a, b and 3a, c, d). Biotite mainly appears as porphyroblasts of 500 μm to 5 mm, exhibiting surfaces crenulated according to two different microfold axes, undulose extinctions, irregular grain boundaries (e.g. Fig. 3d), and Qz and Ab inclusion trails oblique or subparallel to S_2 (marked as S_1 in Fig. 3a, c and d). Garnet also appears as euhedral porphyroblasts, wrapped by the S_2 cleavage (Fig. 3b and c). Sample w13-5 contains large (1–4 mm) garnet grains (~7 vol. %) with lobate grain boundaries, locally rich in quartz inclusions (Figs 2a, 3b and 4a). Sample w13-4 contains sparser (~5 vol. %) and smaller (800 μm–1 mm) garnet grains, showing a 200 μm inclusion-free core, an intermediate inclusion-rich mantle zone with lobate contours and a thinner (*c.* 100 μm wide) inclusion-free rim (Figs 2b, 3c and 4b). The inclusion trails in garnet mimic the folded S_1 (Fig. 3c). Whereas in sample w13-5 garnet is in contact with biotite porphyroblasts (textural equilibrium), in sample w13-4 garnet shares grain boundaries with chlorite (Fig. 3c) but it is not observed in direct contact with biotite (it develops in distant growth sites). Garnet and biotite are associated with ilmenite, elongated in S_1 (w13-5) and S_2 (w13-5 and w13-4) (Figs 2 and 3a–c). Apatite grains of ~10–15 μm are observed as inclusions in garnet and in the matrix in sample w13-5, and only in the matrix in sample w13-4.

Sample w13-3 is less deformed than samples w13-5 and w13-4. The early Wm + Chl-bearing S_1–S_2 cleavage is almost completely overprinted by euhedral grains of Bt, Grt, Ilm, Wm and Chl (Figs 2c and 3e, f). Biotite porphyroblasts (~4 vol. %) exhibit irregular grain boundaries and are partially overgrown by white mica

Table 1: Summary of the principal characteristic of the studied samples

Sample	Petrography	*P–T* method	*P–T*	Aln features	Age (Ma)
W13-5	Deformed (S_1 and S_2)	Peak conditions: forward thermodynamic modelling	597°C, 10 kbar	In garnet and in matrix, 2 thin Ep rings	Too small or inclusion-rich to be successfully dated
	Bt: ∼10 vol. %, porphyroblasts in contact with Grt	Ti-in-biotite	590 ± 24°C		
	Grt: 7 vol. %, porphyroblasts 1–4 mm				
W13-4	Deformed (S_1, S_2)	Peak conditions: forward thermodynamic modelling	575°C	Only in matrix	179·8 ± 8·7
	Bt: 8 vol. %, crenulated porphyroblasts, not in contact with Grt	Ti-in-biotite	550 ± 24°C	3 sharp rings around Aln: R1: REE, Y, Th-rich; R2: Y-rich, LREE-depleted; R3: REE-rich, Y-depleted	
	Grt: ∼4 vol. %, porphyroblasts of 800–1 mm, texturally zoned			Secondary inclusion-like dissolutions	
W13-3	Poorly deformed mineral assemblage overprinting relicts of S_2 cleavage	Peak conditions: forward thermodynamic modelling	570°C, 8 kbar	In garnet and in the matrix	203·2 ± 4·2
	Bt: ∼4 vol. % porphyroblasts	Ti-in-biotite	576 ± 24°C	2 progressive rings: Ep1: REE+Y-rich Ep; Ep2: clinozoisite	
	Grt: >10 vol. %, 3–4 mm, porphyroblasts fractured and unzoned				
W13-2	Deformed (S_1 transposed in S_2)	Ti-in-biotite	573–581 ± 24°C	Aln in matrix	182·7 ± 5·8
	Bt: ∼4–5 vol. %, porphyroblasts strongly chloritized	Chl–Wm multi-equilibrium	350–410°C, 3 ± 1 kbar	Relicts of Aln rings	
	No garnet			Inclusion-like dissolutions	
	Late Wm–Chl assemblage			Aln → Mnz where rings are absent	
W13-1	Highly deformed (mylonite)	Chl–Wm multi-equilibrium	400°C, 4·5 ± 1 kbar	Aln in matrix	Aln1 (Al-depleted): 200·3 ± 7·3
	Only Chl, Wm and Qz	RSCM	528 ± 30°C	One weak Al-depleted ring (locally)	Aln2: 180·3 ± 13·5
	Pseudomorphs of Bt porphyroblasts			Aln → Mnz	
				Mnz aligned along the main schistosity	

Aln, allanite; RSCM, Raman spectroscopy on carbonaceous material; GS, greenschist facies. *P–T* conditions (when not otherwise specified) refer to the maximum pressure and temperature conditions reached by the sample (not necessarily simultaneously).

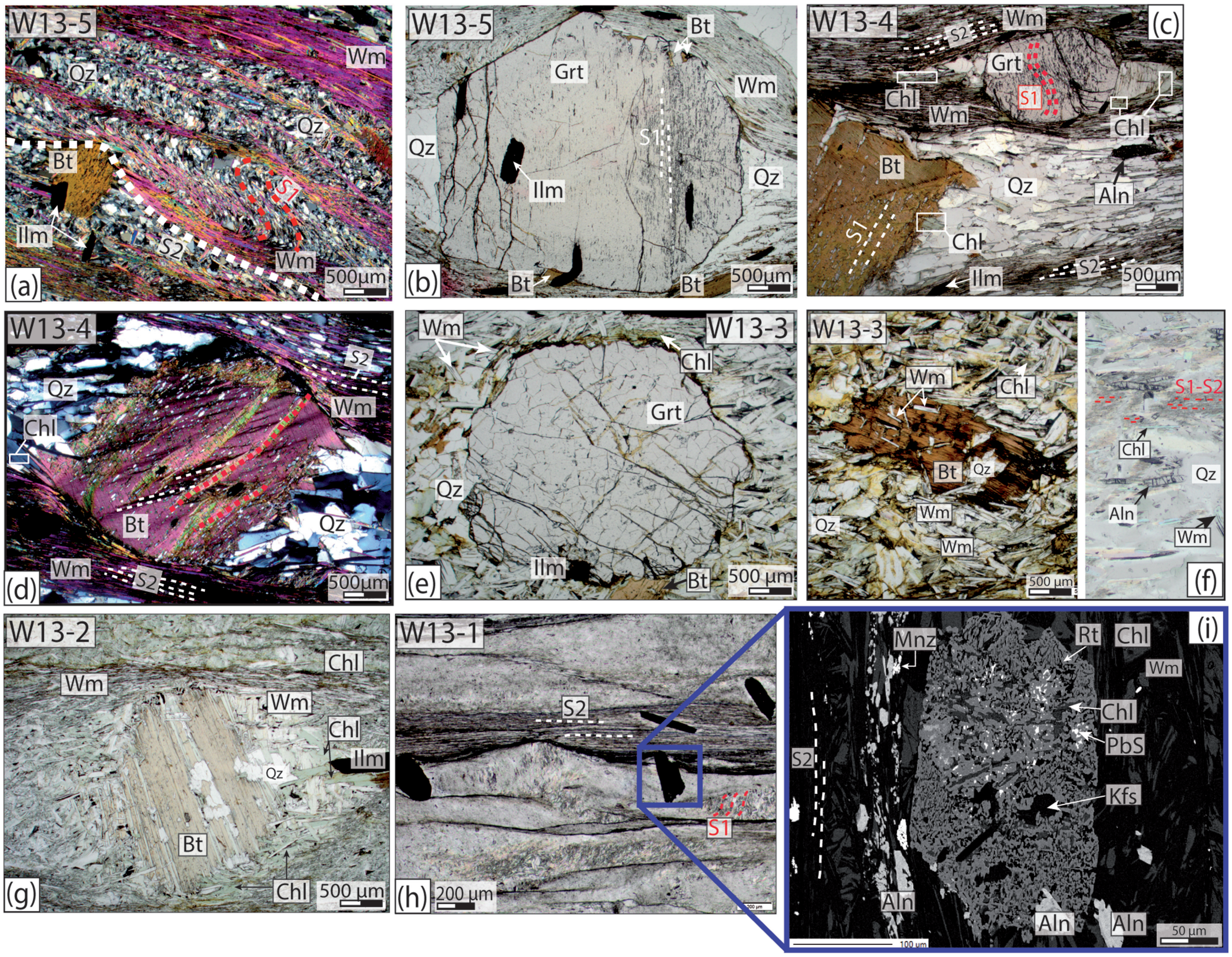

Fig. 3. Photomicrographs of the studied samples. (a) Sample w13-5 (under crossed polars). (b) Garnet porphyroblast wrapped in the white mica-bearing S_2 cleavage in sample w13-5. (c) Deformed garnet and biotite porphyroblasts in sample w13-4, preserving the folded S_1 cleavage. (d) Biotite porphyroblast in sample w13-4 (under crossed polars) showing the surface crenulated along two microfold axes. (e) Inclusion-free porphyroblast of garnet in sample w13-3. (f) Biotite porphyroblast (partially resorbed) in sample w13-3 (left) and S_1–S_2 Wm + Chl + Aln-bearing cleavage almost totally overprinted by the growth of large grains (right). (g) Partially resorbed porphyroblast of crenulated biotite in the retrogressed sample w13-2. (h) Mylonite w13-1. (i) Backscattered electron image (BSE) of the dark porphyroblast in (h) from sample w13-1, made up of aggregates of Rt + Chl + Kfs ± Pyrite ± Wm.

(100–200 µm; Fig. 2f). Garnet shows rims in sharp contact with biotite (Fig. 3e). Compared with the samples described above, garnet grains (6–10 vol. %) are larger (3–4 mm), inclusion-free, texturally homogeneous, fractured and locally surrounded by chlorite (Figs 2c, 3e, 4c and 5e). Apatite grains of 10–25 µm size are observed as inclusions in garnet (Fig. 4e) and in the matrix.

Approaching the Wenchuan shear zone the garnet–biotite-bearing assemblage becomes progressively retrogressed under greenschist-facies conditions. In sample w13-2 garnet is no longer present (Fig. 2d). Biotite (~4 vol. %) appears as porphyroblasts wrapped by S_2, rich in albite inclusions oblique to S_2, and extensively replaced by euhedral Chl + Wm grains (100–200 µm; Fig. 2g). Sample w13-1, collected within the WSZ, is a mylonite comprising Chl + Wm + Qz + Ab (+ Aln + Mnz as accessory phases), with an extremely tight and pervasive cleavage (Figs 2e and 3h) and dark oxide-like porphyroblasts wrapped in the main foliation (Fig. 3h and i). Backscattered electron (BSE) images reveal that the pseudomorphs consist of Rt + Chl + KFs (± Ms ± Pyrite; Fig. 3i), suggesting biotite breakdown owing to retrogression (Stober & Bucher, 2002).

In all samples, the S_1 and S_2 cleavages are interpreted as prograde to peak microstructures, as for units located ~40 km northeastward in an equivalent structural position (Dirks *et al.*, 1994; Airaghi *et al.*, 2017*b*, 2018*a*, 2018*b*)). Garnet and biotite are the index minerals of the amphibolite-facies metamorphism. Microtextures indicate that biotite is pre- to syn-garnet in samples w13-5 and w13-3, whereas in sample w13-4 it is syn- to post-garnet growth, as indicated by the different geometry of inclusion trails and the absence of textural equilibrium. The euhedral shape of minerals in sample w13-3 suggests an extensive equilibration of the mineral assemblage at conditions post-dating the

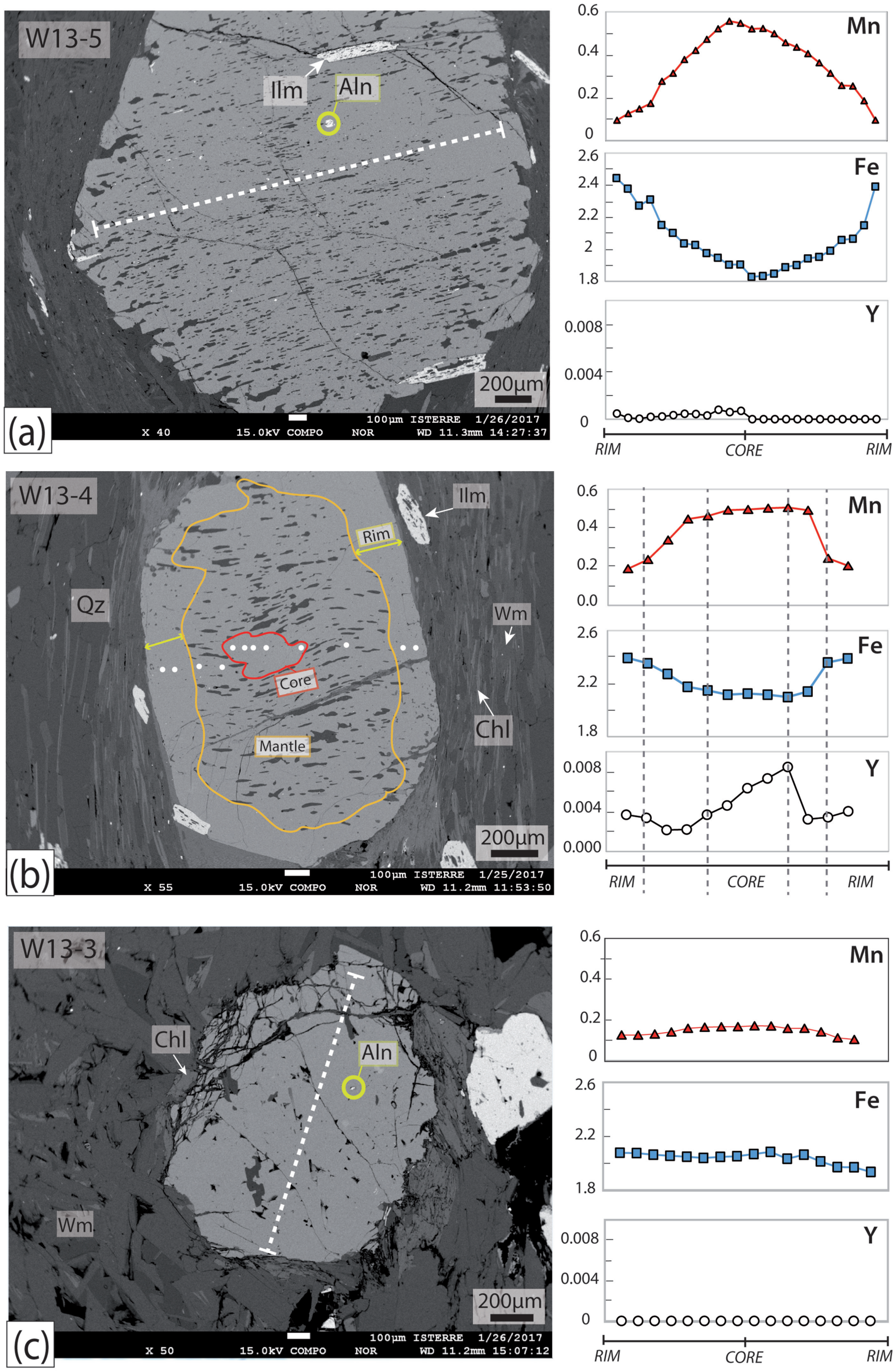

Fig. 4. Representative chemical analyses of garnet in samples w13-5 (a), w13-4 (b) and w13-3 (c). Left column: BSE images of analyzed garnet porphyroblasts. In sample w13-5 analyses were acquired along the profile (white dashed line) after each 110 µm, and in sample w13-3 after each 80 µm. The distance between point analyses in the garnet of sample w13-4 (white dots) varies to avoid Qz inclusions. Right column: Mn, Fe and Y (a.p.f.u.) contents measured along the profiles and points.

S_2-forming stage. In the retrogressed sample w13-2 biotite is syn-S_2.

ANALYTICAL METHODS

Bulk-rock composition

Bulk-rock and mineral chemical compositions were determined to unravel variations in the REE + Y content between samples and to determine their metamorphic conditions of formation (*P*–*T*). Whole-rock major and trace element compositions were obtained by inductively coupled plasma optical emission spectrometry (ICP-OES) and laser ablation inductively coupled plasma mass spectrometry (LA-ICP-MS) using fused glass beads, respectively, at the Bureau Veritas Commodities Canada Ltd (Vancouver, Canada).

Mineral characterization

The chemical compositions of Grt, Bt, Chl and Wm were obtained by electron probe microanalysis (EPMA) using a JEOL JXA-8230 instrument at the Institut des Sciences de la Terre (ISTerre, Grenoble, France), using 15 keV as accelerating voltage, a 12 nA specimen current, and a beam size of 1 µm. The major element and Y concentrations in garnet (at least three grains per sample) of fresh garnet-bearing metapelites (w13-5, w13-4 and w13-3) were analyzed along core-to-rim transects and via X-ray maps to decipher the crystallization sequence of garnet and allanite. Transects were obtained with an 15 keV accelerating voltage and 500 nA beam current. X-ray maps of garnet were made at 20 keV, 200 nA with a dwell time of 200 ms. Maps were transformed into maps of oxide weight percentage with the software XMapTools 2.3.1 (Lanari *et al.*, 2014, 2018).

In sample w13-3 several garnet grains (>2 mm diameter) were too large to be mapped by EPMA in a convenient time for acquisition. They were therefore analyzed with an EDAX Eagle III X-ray fluorescence (XRF) spectrometer, equipped with a Rh anode operating at 20 keV and 200 µA, at ISTerre. XRF maps were acquired with a 30 µm beam, 24 µm step interval in both map directions and a dwell time of 500 ms per pixel.

Allanite grains and later alteration to monazite were identified in polished thin sections using BSE images. The chemical composition of allanite was analyzed by EPMA at 15 keV, 20 nA, with a beam size ≤1 µm. Allanite X-ray compositional maps were acquired using EPMA at a 300 nA specimen current with a dwell time of 200 ms. Monazite observed in retrogressed samples w13-2 and w13-1 was analyzed by EPMA at 15 keV, 200 nA, using a beam size <1 µm. The detailed protocol for monazite analysis is given in Supplementary Data S1 (supplementary data are available for downloading at http://www.petrology.oxfordjournals.org). An attempt at U–Th/Pb monazite dating by EPMA was carried out, but Pb concentrations in all monazite grains were below the detection limit (~130 ppm), which prevented us from obtaining quantitative ages, but allowed us to estimate an upper age limit of 90–100 Ma (see Supplementary Data S1; Montel *et al.*, 2000).

Raman spectroscopy on carbonaceous material (RSCM) was used to analyze the organic material in sample w13-1, employing a Renishaw InVia Reflex microspectrometer (ENS Paris, France) equipped with a 514 nm Spectra Physics diode laser in circular polarization, at a laser power of 12 mW. Fifteen spectra were acquired for the sample and processed using the software Peakfit©.

U–Th/Pb allanite geochronology

In situ U–Pb/Th dating of allanite was performed by LA-ICP-MS on the same polished thin sections as used for the microstructural, petrological and thermobarometric studies at the Institute of Geological Sciences (University of Bern) with a GeoLas Pro & 93 nm ArF excimer laser ablation system coupled with an ELAN DRC-e quadrupole ICP-MS (QMS) system. The data acquisition procedure and the data reduction technique have been summarized by Burn *et al.* (2017). Aluminium was also measured by LA-ICP-MS and quantified using the glass SRM610 from NIST, and Si was used as internal standard. The laser operating conditions were 9 Hz repetition rate and 2·5 J cm^{-2} fluence, with a beam diameter of 24 µm. The analyses were bracketed with the zircon reference material Plešovice (Sláma *et al.*, 2008) used as a primary standard and the reference materials BONA^{b} (Burn *et al.*, 2017) and TARA (Gregory *et al.*, 2007) to check the accuracy of each analytical session. Standards were measured after every 10 sample analyses. One analysis consisted of 60 s of measurement preceded by 20 s of washout, 40 s of background counting and ~10 s of pre-ablation of the surface (carried out with a laser beam diameter of 32 µm to avoid contamination by surface common lead). Data were reduced using the non-matrix-matched standardization procedure of the in-house software package Trinity (Burn *et al.*, 2017).

An average of 10–20 analyses were performed for each sample. Grains were chosen on the basis of their size (>30 µm), in domains away from epidote rims. Analyses exhibiting age zoning were discarded during the integration process and only flat age signals were selected. U–Pb and Th values from several allanite grains in the same sample were processed as a single population to retrieve a unique weighted mean age. This strategy was supported by the petrological observations showing that allanite grains shared similar characteristics within a specific sample.

RESULTS

Bulk-rock and mineral compositions

Bulk-rock major and REE chemical compositions are reported in Table 2. Sample w13-3 is significantly enriched in CaO (3·3 wt %) compared with other metapelites (0·19–0·59 wt %). The total REE + Y content is similar in samples w13-1, w13-4 and w13-5 (202–250 ppm); w13-2 and w13-3 have higher REE and Y contents (372 and 333 ppm).

Representative chemical analyses of minerals are listed in Table 3. Garnet in sample w13-5 exhibits bell-shaped compositional zoning, with a progressive decrease in both Mn and Ca and an associated increase in Fe and Mg from the core through the mantle to the rim (Fig. 4a). The Y content is close or below the EPMA detection limit, estimated at ~90 ppm (<0·0007 a.p.f.u.; Fig. 4a and Table 3). Quantitative maps show dissolution features and lobate chemical zoning around inclusions (Fig. 5a). In garnet of sample w13-4 the Mn content also decreases from core to rim, whereas the contents of both Fe and Mg increase (Figs 4b and 5c). The shape of the zoning profile comprises a flat core area of ~600 µm and a mantle to rim region of ~200 µm in which composition varies more rapidly (Figs 4b and 5c).

Table 2: Bulk-rock composition for the studied samples

Sample:	W13-1	w13-2	W13-3	W13-4	W13-5
Longitude:	103·575	103·576	103·57	103·565	103·551
Latitude:	31·477	31·494	31·504	31·51	31·518
Major oxide (%)					
SiO_2	46·05	45·05	41·24	60·05	64·10
Al_2O_3	25·94	26·08	28·08	19·36	18·45
Fe_2O_3	11·00	9·75	9·02	7·49	6·05
MgO	3·75	4·01	3·18	2·86	1·36
CaO	0·19	0·77	3·3	0·37	0·59
Na_2O	0·26	0·57	0·54	0·93	2·32
K_2O	5·99	6·62	6·7	4·53	3·93
TiO_2	1·09	1·03	1·1	0·69	0·75
P_2O_5	0·05	0·10	0·42	0·10	0·05
MnO	0·05	0·09	0·39	0·07	0·23
Cr_2O_3	0·021	0·023	0·02	0·014	0·009
LOI	5·3	5·6	5·7	3·3	1·9
Sum oxide	99·77	93·97	99·76	99·84	97·78
Ca/Ca Shaw	0·09	0·17	1·54	0·17	0·22
Al/Al Shaw	1·56	1·49	1·69	1·17	0·91
CaO/Na_2O	0·73	1·35	6·11	0·40	0·25
Rare earth element (ppm)					
Y	32·9	43	50·6	25·6	34·7
La	36·5	78·3	60·1	44·8	49·1
Ce	69·5	142	115·9	84·4	97·4
Pr	7·91	15·56	13·38	9·73	9·47
Nd	28	54·5	49·3	34·6	31·5
Sm	5·08	9·24	8·98	6·06	5·54
Eu	1·04	1·92	1·68	1·21	0·81
Gd	5·21	7·83	8·23	5·44	5
Tb	0·91	1·2	1·28	0·81	0·87
Dy	5·66	7·05	7·47	4·78	5·87
Ho	1·24	1·49	1·59	0·96	1·4
Er	3·7	4·45	5·61	2·91	3·78
Tm	0·53	0·68	0·95	0·43	0·56
Yb	3·38	4·23	7	2·69	3·55
Lu	0·54	0·58	1·05	0·43	0·52
REE + Y	202·1	372·03	333·12	224·85	250·07
LREE	141·91	290·36	238·68	173·53	187·47
MREE	11·33	18·99	18·89	12·71	11·35
HREE	15·96	19·68	24·95	13·01	16·55

LOI, loss on ignition (%). Cation ratios 'Shaw' are from Shaw *et al.* (1956).

Garnet also exhibits a weak Ca zoning, which is discordant with the other elements; Ca slightly increases from the garnet core to the mantle and decreases from the mantle to the rim (Table 3). Garnet of sample w13-4 exhibits (1) a core with higher Y content, (2) a Y-poor mantle zone, and (3) a relatively Y-rich rim (Figs 4b and 5d and Table 3). The Y zoning corresponds to the textural zoning observed in the BSE images, but is different from the zoning in Mn, revealing a decoupling between some major and trace element zoning patterns. In sample w13-3, garnet <2 mm has a relatively homogeneous composition in Fe, Ca and Mg (Figs 4c and 5b). The Mn content slightly decreases from core to rim (Fig. 4c), and Y is < ~90 ppm (Fig. 4c and Table 3). The XRF compositional maps of garnet grains >2 mm show zoning features similar to those of smaller garnet grains (Fig. 5e).

The Ti content of biotite slightly increases from core to rim of porphyroblasts in samples w13-3 and w13-5, but it is homogeneous in biotite of sample w13-4 and is irregular in biotite of sample w13-2 (Table 3).

Samples w13-5, w13-3 and w13-1 exhibit a single Wm compositional group (dominant muscovite end-member of 70%; Table 3). By contrast, metapelite w13-2 contains two Wm groups (Table 3): the first (Wm1) includes the cores of white mica grains aligned in the main S_2 cleavage; the second group (Wm2) includes the rims of the Wm grains and late Wm porphyroblasts, and exhibits a lower Si content and X_{Mg} (Table 3). In this sample, two chemical groups of chlorite are also recognized: the first (Chl1) is the product of the breakdown of biotite, whereas the second group (Chl2) is observed in the matrix and shows lower Si and higher Al contents compared with Chl1 (Table 3). In sample w13-1, only one group of chlorite was observed.

***P–T* estimates**

Following Airaghi *et al.* (2017*b*), different thermobarometric approaches (iterative forward and multi-equilibrium thermodynamic modelling, Ti-in-biotite thermometry and RSCM; see Table 1) were combined to investigate the evolution of the mineral assemblages and the mineral compositions along the reconstructed *P–T* trajectory.

Thermodynamic modeling

The metamorphic conditions as well as the sequence of mineral growth were modeled using a two-step approach. First, optimal *P–T* conditions of the successive garnet growth zones were calculated in the three garnet-bearing samples (w13-5, w13-4, w13-3) using the program GrtMod (Lanari & Engi, 2017; Fig. 6a) and the bulk-rock compositions given in Table 2. These *P–T* stages (especially for w13-5, which best preserves the entire metamorphic history) define a prograde trajectory that, if compared with the *P–T* data obtained by Airaghi *et al.* (2017*b*) for the early prograde and post-peak-*P* condition in samples located in an equivalent structural position, can be used to infer a 'representative' *P–T* path (grey line in Fig. 6a). In a second step, the volume fraction of each mineral phase and their chemical compositions were modeled along the representative *P–T* path using THERIAK-DOMINO (de Capitani & Brown, 1987; de Capitani & Petrakakis, 2010). Model predictions were compared with the chemical analyses and with the observed mineral assemblages (Fig. 7 and Supplementary Data Fig. S1). The last updated version of the thermodynamic database of Holland & Powell (1998) was used for phase equilibria modeling with the list of activities provided in Supplementary Data S1. A pure H_2O fluid was assumed to be in excess. Because all these samples contain a significant amount of ilmenite, suggesting reduced conditions, all Fe was assumed to be divalent (e.g. Diener & Powell, 2010; Weller *et al.*, 2013).

In sample w13-5, the chemical composition of the garnet core is predicted at 7·3 kbar, 520°C (uncertainties are reported in Fig. 6a), at a temperature higher than the one predicted for the appearance of garnet in the

Table 3: Representative chemical analyses of major mineral phases for the studied samples

Sample:	W13-5					W13-4					
Mineral:	Grt			Bt	Wm	Grt			Bt		Wm
Location:	rim	mantle	core			rim	mantle	core	rim	core	
SiO_2	36·62	36·51	36·61	36·46	46·8	36·60	36·60	36·35	36·22	36·51	47·78
TiO_2	0·02	0·09	0·10	1·80	0·23	0·01	0·06	0·06	1·81	1·72	0·30
Al_2O_3	20·61	20·36	20·27	17·59	33·85	20·58	20·35	20·28	18·27	17·86	34·16
FeO	34·94	29·63	27·84	20·58	1·61	35·06	31·85	30·89	20·93	20·29	1·77
MnO	1·82	6·07	8·04	0·03	0·01	2·75	6·45	7·12	0·03	0·00	0·01
MgO	2·20	0·93	0·84	9·56	0·89	1·93	1·55	1·49	9·23	9·44	1·40
CaO	3·44	5·81	5·75	0·02	0	2·68	2·97	2·92	0·06	0·00	0·06
Na_2O	—	—	—	0·04	1·65	—	—	—	0·08	0·12	0·90
K_2O	—	—	—	8·96	9·46	—	—	—	8·36	8·82	9·52
Y_2O_3	0·005	0·020	0·028	—	—	0·170	0·102	0·290	—	—	—
Cations											
Si	2·98	2·99	2·99	2·79	3·14	2·99	2·99	2·99	2·76	2·79	3·15
Ti	0·00	0·01	0·01	0·10	0·01	0·00	0·00	0·00	0·10	0·10	0·01
Al	1·98	1·96	1·95	1·58	2·67	1·98	1·96	1·97	1·64	1·61	2·65
Fe^{2+}	2·38	2·03	1·90	1·31	0·09	2·39	2·18	2·13	1·33	1·30	0·10
Mn	0·13	0·42	0·56	0·00	0·00	0·19	0·45	0·50	0·00	0·00	0·00
Mg	0·27	0·11	0·10	1·09	0·09	0·24	0·19	0·18	1·05	1·07	0·14
Ca	0·30	0·51	0·50	0·00	0·00	0·23	0·26	0·26	0·01	0·00	0·00
Na	0·00	0·00	0·00	0·01	0·21	0·00	0·00	0·00	0·01	0·02	0·11
K	0·00	0·00	0·00	0·87	0·81	0·00	0·00	0·00	0·81	0·86	0·80
Y	0·00	0·00	0·00	—	—	0·004	0·002	0·006	—	—	—
Oxygens	12	12	12	11	11	12	12	12	11	11	11
*X*Mg	0·10	0·05	0·05	0·45	0·50	0·09	0·08	0·08	0·44	0·45	0·58
*X*Pyr	0·09	0·04	0·03	—	—	0·08	0·06	0·06	—	—	—
*X*Alm	0·77	0·66	0·62	—	—	0·78	0·71	0·69	—	—	—
*X*Spe	0·04	0·14	0·18	—	—	0·06	0·15	0·16	—	—	—
*X*Gr	0·10	0·17	0·16	—	—	0·08	0·08	0·08	—	—	—

Sample:	W13-3			W13-2					W13-1	
Mineral:	Grt	Bt	Wm	Bt	Wm		Chl		Chl	Wm
Location:				rim	Wm1	Wm2	Chl1	Chl2		
SiO_2	36·96	36·64	47·45	35·13	47·66	45·55	24·89	26·34	24·74	46·48
TiO_2	0·04	1·59	0·42	1·70	0·28	0·35	0·09	0·08	0·09	0·27
Al_2O_3	20·72	17·52	33·26	17·88	33·06	34·63	22·82	21·31	22·54	35·35
FeO	30·62	17·66	1·64	21·92	2·09	1·89	26·28	27·79	26·79	1·80
MnO	1·84	0·06	0·02	0·11	0·03	0·01	0·14	0·15	0·07	0·01
MgO	1·79	10·91	1·26	10·22	1·38	0·90	13·47	13·71	13·60	0·94
CaO	7·12	0·01	0·01	0·04	0·01	0·01	0·01	0·02	0·02	0·00
Na_2O	n.d.	0·14	0·84	0·11	1·07	1·17	0·02	0·02	0·02	1·33
K_2O	n.d.	8·55	9·56	6·74	9·61	9·22	0·04	0·05	0·03	9·10
Y_2O_3	0·00	—	—	—	—	—	—	—	—	—
Cations										
Si	3·00	2·81	3·17	2·71	3·17	3·08	2·63	2·74	2·62	3·08
Ti	0·00	0·09	0·02	0·10	0·01	0·02	0·01	0·01	0·01	0·01
Al	1·98	1·59	2·62	1·63	2·60	2·76	2·84	2·62	2·81	2·76
Fe^{2+}	2·08	1·13	0·09	1·41	0·12	0·11	2·32	2·42	2·37	0·10
Mn	0·13	0·00	0·00	0·01	0·00	0·00	0·01	0·01	0·01	0·00
Mg	0·22	1·25	0·13	1·18	0·14	0·09	2·12	2·13	2·15	0·09
Ca	0·62	0·00	0·00	0·00	0·00	0·00	0·00	0·00	0·00	0·00
Na	—	0·02	0·11	0·02	0·14	0·15	0·00	0·00	0·00	0·17
K	—	0·84	0·82	0·66	0·82	0·79	0·01	0·01	0·00	0·77
Y	0·00	—	—	—	—	—	—	—	—	—
Oxygens	12	12	11	11	11	11	14	14	14	11
*X*Mg	0·09	0·52	0·58	0·45	0·54	0·46	0·48	0·47	0·47	0·48
*X*Pyr	0·071	—	—	—	—	—	—	—	—	—
*X*Alm	0·68	—	—	—	—	—	—	—	—	—
*X*Spe	0·04	—	—	—	—	—	—	—	—	—
*X*Gr	0·20	—	—	—	—	—	—	—	—	—

For the Y a.p.f.u. content three decimal digits are shown.

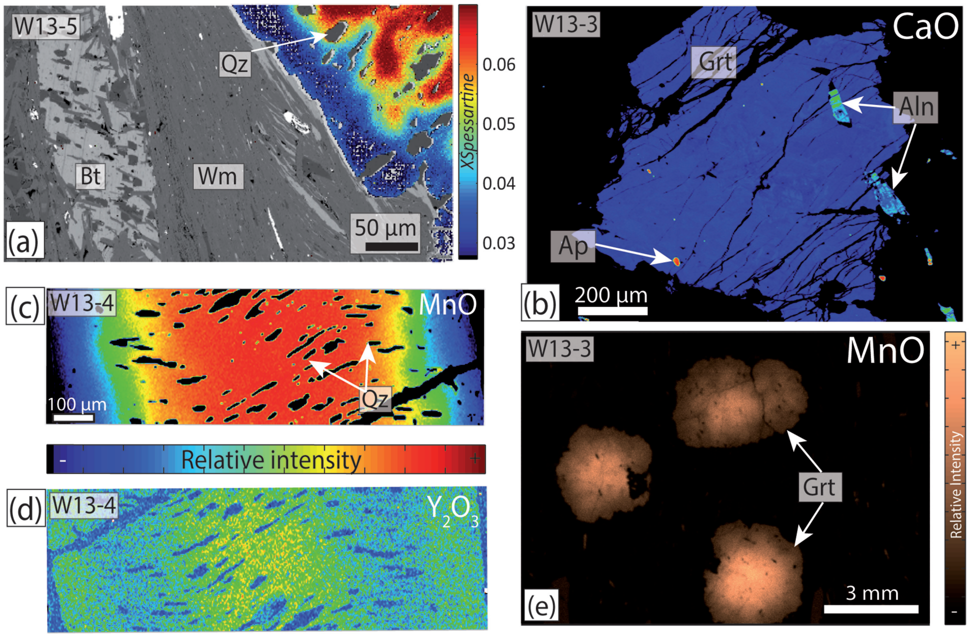

Fig. 5. Compositional maps for garnet obtained by EPMA (a–d) and XRF (e). (a) Spessartine content in a garnet porphyroblast from sample w13-5. Map is superimposed on a BSE image. (b) CaO content in a garnet from sample w13-3 (<2 mm in size). The blue to green mineral phase is an allanite grain with epidote rims included in the garnet. (c) MnO content in a garnet from sample w13-4. (d) Y_2O_3 content of a garnet from sample w13-4. A reference color bar is given in (c). (e) MnO content for garnets >2 mm in sample w13-3.

stable mineral assemblage, suggesting reaction overstepping of ~40°C (Fig. 7a). Garnet mantle and rim compositions, as well as the measured garnet volume proportions, plot at 7·5 kbar, 530°C and 10 kbar, 600°C, respectively. Along the reconstructed *P*–*T* path (grey line in Fig. 6a), biotite is predicted to be stable before garnet nucleation, but the main episode of growth occurs when garnet becomes stable at ~520°C. The Si contents in biotite and white mica correspond to the values predicted by the model at ~520°C (Supplementary Data Fig. S1).

In sample w13-4, optimal solutions for the different stages of garnet growth with high residuals values were found at similar *T* (Fig. 6a), but at lower *P* (around 5–6 kbar). As these probably reflect a bulk-composition effect (see below) rather than real depth differences, only the temperature information of garnet growth is used in the following (shown as vertical dashed lines in Fig. 6a). Temperature conditions were inferred using the Fe–Mg exchange reactions (Fig. 7b). The lowest temperature at which garnet cores are predicted to be stable is ~520°C. Mantle and rim compositions are predicted to be stable at 550°C and 575°C, respectively (Fig. 7b). In this sample, biotite is predicted to become stable along with garnet, whereas the main episode of growth takes place later at ~560–575°C (Fig. 7b).

In sample w13-3, garnet chemical composition and modal abundance (>10 vol. %) are predicted at 570°C, 8 kbar (Fig. 6a). Biotite mainly grows before garnet (Fig. 7c), where the predicted Si content as well as the Si in Wm best fit the measured values (Supplementary Data Fig. S1). For this sample, the evolution of the volume fraction of each mineral phase and chemical composition was modeled to the point of garnet appearance, as microstructures make it difficult to assess if garnet grew during a prograde stage or near the metamorphic peak.

Additional thermobarometric constraints

Phase equilibria modeling was coupled with Ti-in-biotite thermometry (Henry *et al.*, 2005) in all samples containing this mineral. Calculated temperatures are summarized in Table 1. The temperature variations observed in sample w13-2 (573–581 ± 24°C) are associated with the Ti content of the different biotite domains.

The peak conditions (T_{max}) experienced by sample w13-1, the only one depleted in biotite and enriched in organic material, were estimated by RSCM with the calibration of Beyssac *et al.* (2002), yielding a T_{max} of 528 ± 30°C.

In garnet-depleted samples (w13-2, w13-1), a multi-equilibrium approach combining the thermodynamic models of Vidal *et al.* (2005, 2006) and Dubacq *et al.* (2010) was applied to constrain the metamorphic conditions of the Wm–Chl–Qz greenschist assemblage. Optimal *P*–*T* conditions were estimated along the *P*–*T* equilibrium curves of white mica at the *T* of chlorite assuming chemical equilibrium, following the procedures of Lanari *et al.* (2012, 2013) and Airaghi *et al.* (2017*b*). Multi-equilibrium thermobarometry indicates *P*–*T* conditions for the Wm2–Chl2–Qz assemblage in sample w13-2 at 360–410°C, 3 ± 1 kbar (black frame in Fig. 6b). Equilibrium conditions of pairs of Chl2–Wm2 analyses were also tested simultaneously as an

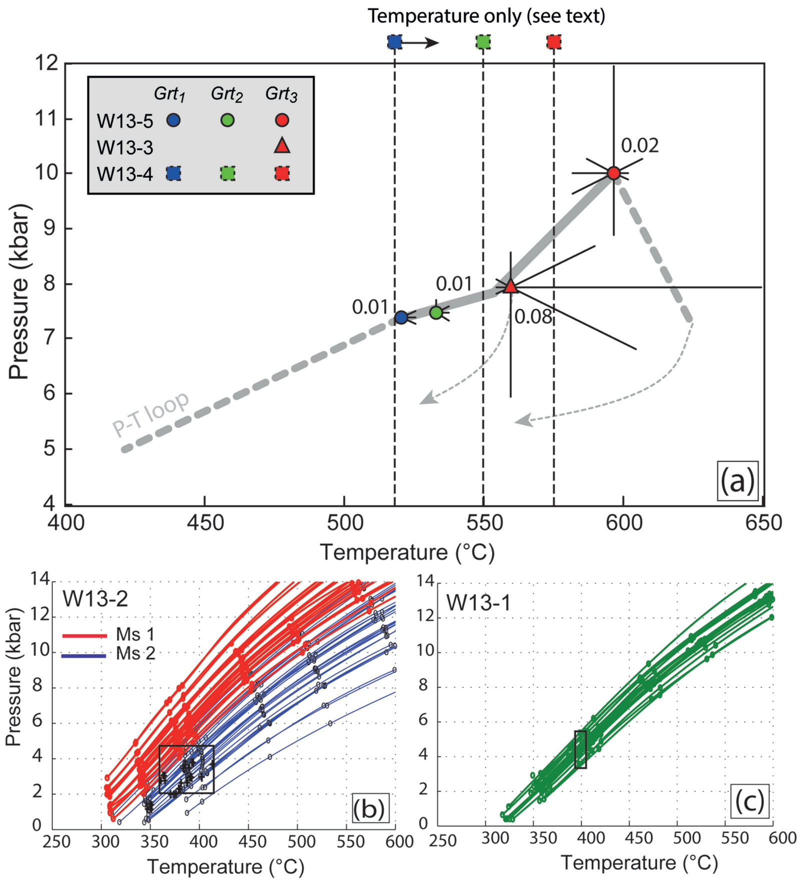

Fig. 6. Thermobarometric results. (a) *P–T* conditions of garnet growth in samples w13-5, w13-4 and w13-3 calculated using the GrtMod fraction crystallization model. Grt1, garnet core; Grt2, garnet mantle; Grt3, garnet rims. Errors (continuous black lines) are estimated using the auto-refinement procedure provided in GrtMod and a residual variation (C_0) of ±1·5 corresponding to the uncertainty resulting from the EPMA chemical analyses. Continuous grey line is the *P–T* loop retrieved from garnet conditions used for the modeling of Fig. 7. Grey dashed line is the extrapolated portion of the *P–T* loop used following Airaghi *et al.* (2017*b*). (b, c) *P–T* lines for white mica in retrogressed samples w13-2 and w13-1 calculated with the multi-equilibrium approach. Black frames: *P–T* conditions of the greenschist assemblages. Black crosses in (b) represent the equilibrium conditions calculated simultaneously for pairs of white mica and chlorite analyses in sample w13-2.

independent check (see Airaghi *et al.*, 2017*b*, for details), and yielded results of 3 ± 1 kbar, 350–410°C, with three outliers below 2 kbar (black crosses in Fig. 6b). In sample w13-1, a lack of convergence among the four equilibria involving Chl, Qz and H_2O was observed and was interpreted as suggestive of temperatures >400–450°C (Lanari *et al.*, 2012). Fixing *T* at 400°C, the pressure for the Wm-bearing assemblage was estimated at 4·5 ± 1 kbar (Fig. 6c, conditions of mylonitization).

Texture and composition of REE minerals

The REE and Y contents of allanite are similar in all samples (Table 4), but significant differences exist in the texture and composition between allanite rims in fresh Grt–Bt metapelites and allanite in retrogressed samples (Table 4 and Fig. 8).

Allanite in garnet–biotite metapelites

In sample w13-5, only few allanite grains (<150 µm in size) were observed as inclusions in garnet porphyroblasts (quartz inclusion-rich allanite) or stretched in the main S_2 cleavage in the matrix (inclusion-free allanite) (Figs 4a and 8a). Allanite exhibits homogeneous light REE (LREE) contents (Table 4), and is surrounded by two thin epidote rims ~5 µm wide (inset in Fig. 8a).

In sample w13-4, allanite exhibits the most complex textures with regard to the number of rims and inclusions. Allanite is observed only in the matrix, where it appears as subhedral grains (100–150 µm large) elongated in the main S_2 cleavage (Fig. 8b and c). Allanite has a homogeneous composition in REE and Y and is surrounded by three generations of rims (Figs 8c and 9a). The first rim R1 is <5 µm wide and enriched in REE (+ Y) and Th compared with the allanite core (Fig. 9a). R1 is preserved only locally and is therefore difficult to analyze quantitatively (possibly REE carbonates or phosphates). Where R1 has been totally resorbed, quartz fills the space between the allanite and its second rim, R2 (Fig. 9a). R2 is 20–25 µm wide and corresponds to a REE-rich epidote (REE <0·5 a.p.f.u.) enriched in Y and

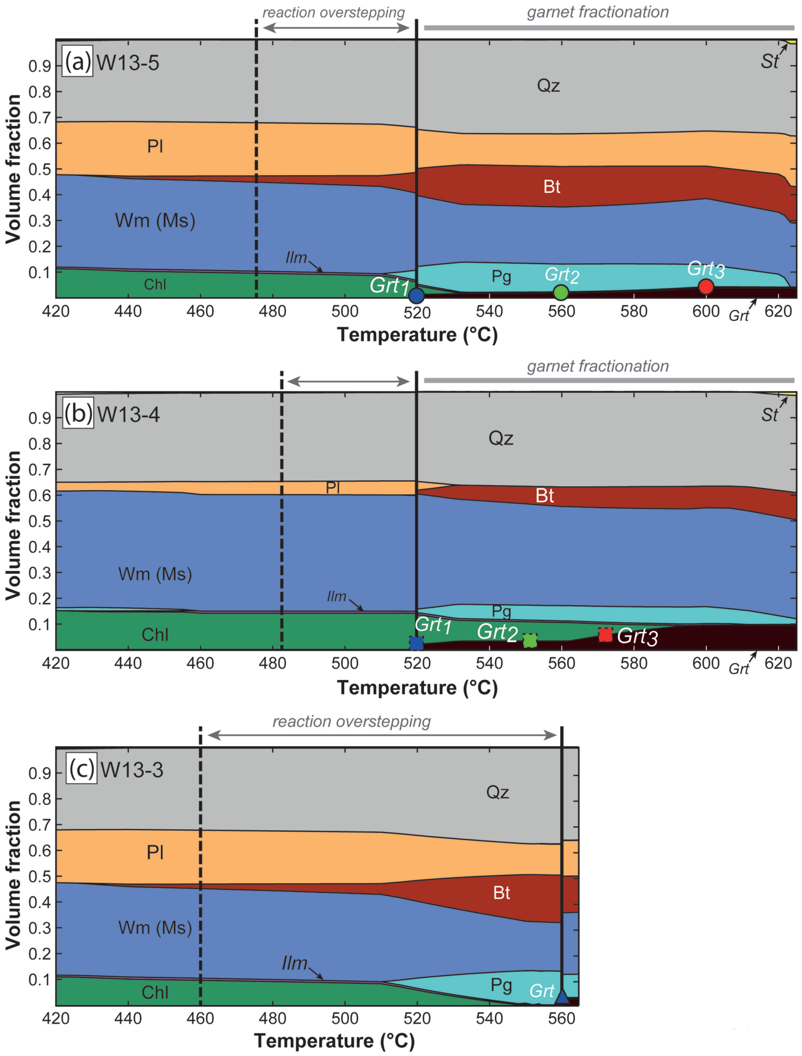

Fig. 7. Variations of mineral volume fraction calculated along the *P–T* loop of Fig. 6 using a garnet fractionation model. Colored dots (w13-5), squares (w13-4) and triangle (w13-3) indicate the conditions obtained for garnet core (green) (blue), mantle and rims (red), respectively.

depleted in LREE relative to the allanite core (and R1, Table 4). The third rim, R3 (Fig. 9a), is a thin (5–10 μm wide) REE-rich epidote, enriched in Y compared with the allanite, but Y-depleted and LREE-enriched compared with R2 (Table 4). Concentric zoning is observed in R3 as shown by the Ca X-ray maps (Fig. 9a). The boundaries between the allanite and R1 and between R1 and R2 are sharp, whereas that between R2 and R3 is gradual.

In this same sample, w13-4, allanite contains abundant 'inclusions' (20–30 μm in size), oblique to S_2 in basal sections and subparallel to S_2 in longitudinal sections (Figs 8b, c and 9a). Inclusions consist of quartz surrounded by successive rims of epidote ('trail' T2 and T3 in Table 4), with compositions overlapping those of R2 and R3 (Fig. 9a), and microstructurally cross the boundary between allanite core and rims.

In sample w13-3, allanite grains are either shielded as inclusions in garnet (Figs 4c, 5b and 8d) or elongated in the early S_1–S_2 cleavage (Fig. 8e). In both microstructural positions, allanite occurs as inclusion-free, sub-euhedral grains (50 μm wide, 600 μm long), surrounded by two successive REE-bearing epidote rims. The allanite core has a homogeneous Y and LREE content (Fig. 9b and Table 4). The first rim of REE-rich epidote (Ep1) is enriched in Y and depleted in La, Nd, Sr and Ce compared with allanite. The second rim (Ep2) exhibits the composition of LREE-enriched and Y-depleted clinozoisite (Y < 568 ppm). The transition from allanite to Ep1 is sharp, whereas that between Ep1 and Ep2 is gradual. Allanite in the matrix is fractured and segmented. It should be noted that allanite is observed as inclusions in garnet only in samples w13-5 and w13-3.

Allanite in retrogressed samples

In both samples w13-2 and w13-1, allanite grains are generally smaller than in the fresh Grt–Bt metapelites

Table 4: Representative chemical compositions for allanite (Aln)

Sample:		w13-1		w13-2	w13-3			w13-4					w13-5
Position:		Aln	Ep1	Aln	Aln	Ep1	Ep2	Aln	R2	T2	R3	T3	Aln
Analysis:	d.l.	all15-7	all10-1	all1-3	all7	all14-2	all14-3	all7-2	all7-5	all16-2	all3-3	all6-2	all2
SiO_2	521	31·00	34·07	31·83	31·55	36·02	38·39	31·72	35·63	35·45	33·50	34·93	31·96
TiO_2	220	0·12	0·05	0·17	0·16	0·05	0·12	0·12	0·04	0·05	0·07	0·06	0·07
ThO_2	391	0·58	1·46	0·78	0·47	0·26	0·02	1·52	0·16	0·27	2·15	1·24	0·25
UO_2	556	0·03	0·19	0·00	0·00	0·08	0·04	0·04	0·07	0·05	0·44	0·32	0·11
Al_2O_3	469	17·65	22·18	18·75	18·55	25·21	28·81	18·85	24·56	24·48	21·81	21·99	20·46
Y_2O_3	568	0·12	2·03	0·20	0·19	0·80	0·00	0·34	5·88	5·12	0·45	0·42	0·21
La_2O_3	615	5·65	2·36	4·61	5·91	1·54	0·06	5·22	0·27	0·65	2·90	3·11	4·85
Ce_2O_3	520	11·21	4·80	10·70	11·10	3·07	0·15	9·75	0·45	1·15	5·65	6·13	9·72
Pr_2O_3	1094	1·29	0·52	1·39	1·30	0·32	0·04	1·11	0·00	0·13	0·59	0·67	0·82
Nd_2O_3	530	4·43	2·14	4·74	4·17	1·30	0·08	3·90	0·26	0·56	2·55	2·59	3·31
Sm_2O_3	1127	0·56	0·40	0·70	0·46	0·12	0·00	0·59	0·14	0·21	0·56	0·51	0·45
Gd_2O_3	1410	0·19	0·73	0·45	0·35	0·14	0·07	0·36	0·70	0·69	0·72	0·61	0·35
MgO	279	0·11	0·13	0·15	0·11	0·08	0·00	0·23	0·12	0·12	0·27	0·20	0·46
CaO	254	10·50	14·99	10·62	10·84	19·10	23·95	11·33	17·46	17·28	14·99	15·04	12·59
MnO	367	0·19	0·22	0·54	0·53	0·38	0·07	0·45	0·53	0·59	0·07	0·14	0·03
FeO	424	10·92	7·23	11·59	10·65	3·76	0·00	9·56	5·31	5·25	6·31	8·08	8·33
Fe_2O_3	—	0·78	2·28	0·87	0·29	3·67	5·19	2·21	3·32	3·54	3·41	0·96	1·89
SrO	1352·00	0·00	0·00	0·00	0·00	0·00	0·00	0·00	0·00	0·00	0·00	0·00	0·00
PbO	775	0·00	0·04	0·00	0·01	0·00	0·04	0·02	0·01	0·04	0·04	0·12	0·03
Na_2O	—	0·00	0·00	0·00	0·00	0·00	0·00	0·00	0·00	0·00	0·00	0·00	0·00
H_2O	—	1·53	1·68	—	1·57	1·79	1·92	1·59	1·77	1·77	1·67	1·70	1·61
Total	—	96·88	97·53	97·21	98·21	97·69	98·94	98·92	96·68	97·40	98·18	98·81	97·51
Cations													
Si		3·03	3·03	3·02	3·02	3·02	3·00	3·00	3·01	3·00	3·01	3·09	2·97
Ti		0·01	0·00	0·01	0·01	0·00	0·01	0·01	0·00	0·00	0·00	0·00	0·01
Th		0·01	0·03	0·02	0·01	0·00	0·00	0·03	0·00	0·01	0·04	0·02	0·01
U		0·00	0·00	0·00	0·00	0·00	0·00	0·00	0·00	0·00	0·01	0·01	0·00
Al		2·03	2·33	2·10	2·09	2·49	2·66	2·10	2·45	2·44	2·31	2·29	2·24
Y		0·01	0·10	0·01	0·01	0·04	0·00	0·02	0·26	0·23	0·02	0·02	0·01
La		0·20	0·08	0·16	0·21	0·05	0·00	0·18	0·01	0·02	0·10	0·10	0·17
Ce		0·40	0·16	0·37	0·39	0·09	0·00	0·34	0·01	0·04	0·19	0·20	0·33
Pr		0·05	0·02	0·05	0·05	0·01	0·00	0·04	0·00	0·00	0·02	0·02	0·03
Nd		0·15	0·07	0·16	0·14	0·04	0·00	0·13	0·01	0·02	0·08	0·08	0·11
Sm		0·02	0·01	0·02	0·02	0·00	0·00	0·02	0·00	0·01	0·02	0·02	0·01
Gd		0·01	0·02	0·01	0·01	0·00	0·00	0·01	0·02	0·02	0·02	0·02	0·01
Mg		0·02	0·02	0·02	0·02	0·01	0·00	0·03	0·01	0·02	0·04	0·03	0·06
Ca		1·10	1·43	1·08	1·11	1·71	2·01	1·15	1·58	1·57	1·44	1·43	1·25
Mn		0·02	0·02	0·04	0·04	0·03	0·00	0·04	0·04	0·04	0·01	0·01	0·00
Fe^{2+}		0·89	0·54	0·90	0·85	0·26	0·00	0·75	0·37	0·37	0·47	0·60	0·65
Fe^{3+}		0·06	0·15	0·02	0·02	0·23	0·31	0·16	0·21	0·23	0·23	0·06	0·13
Sr		0·00	0·00	0·00	0·00	0·00	0·00	0·00	0·00	0·00	0·00	0·00	0·00
Pb		0·00	0·00	0·00	0·00	0·00	0·00	0·00	0·00	0·00	0·00	0·00	0·00
Na		0·00	0·00	0·00	0·00	0·00	0·00	0·00	0·00	0·00	0·00	0·00	0·00
ΣREE		0·84	0·45	0·79	0·82	0·23	0·01	0·74	0·32	0·33	0·44	0·46	0·67
*X*LREE		0·78	0·56	0·74	0·78	0·65	0·65	0·76	0·07	0·18	0·68	0·70	0·78
*X*MREE		0·21	0·23	0·25	0·21	0·20	0·35	0·22	0·10	0·13	0·27	0·25	0·20
*X*HREE		0·01	0·21	0·01	0·01	0·15	0·00	0·02	0·83	0·69	0·05	0·04	0·02
Th/U		15·25	7·34	—	100·50	3·14	—	27·57	2·30	4·89	4·79	3·82	2·25

Ep1, Ep2, R2 and R2 are epidote rings surrounding allanite (see the text for details). T2 and T3 are rims around 'Trails of inclusions' within allanite grains of sample w13-4. Detection limits (d.l.) are expressed in ppm.

(on average <50 μm, occasionally >100 μm). In sample w13-2, allanite is elongated in the main S_2 cleavage. Grains are generally fragmented (fragment size ~50 μm) and fractured. They exhibit lobate grain boundaries suggestive of allanite resorption (Fig. 8f and g). Allanite breakdown into Mnz propagates in fractures and from grain boundaries towards the core of allanite (Fig. 8f). Only rare evidence of tiny epidote rims (<2 μm wide; too small for EMPA) was observed around two large (>100 μm) allanite grains (Fig. 8f and g).

In sample w13-1, allanite occurs in aggregates of small grains (20–60 μm) elongated in the main foliation (Fig. 8h) or as isolated grains of 50–60 μm in size stretched or superimposed on the S_2 cleavage (Fig. 8i). The composition of allanite is consistent throughout the sample (Table 4). BSE images and EPMA reveal the existence of thin (<8 μm) epidote rims located around the isolated allanite grains, which are depleted in Al (Al <2·10 a.p.f.u.) and LREE, but enriched in Y compared with allanite cores (Table 4). Allanite is partially replaced by monazite 10–20 μm in size (inset in Fig. 8h and i). Monazite grains are elongated in the main foliation (Fig. 8h) and have Pb contents below the EPMA detection limit of 130 ppm (Table 5). Based on this

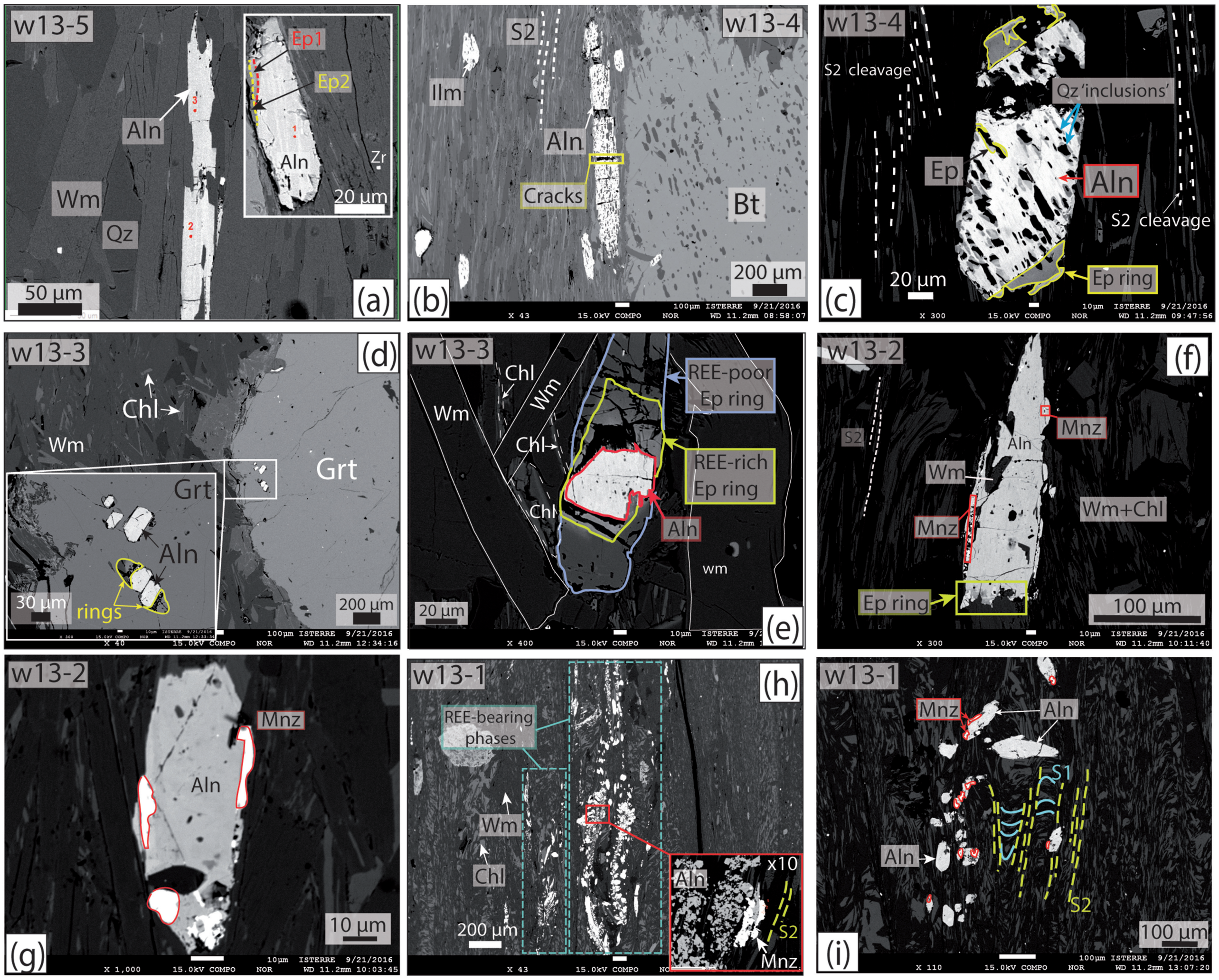

Fig. 8. Backscattered electron images of allanite in the different samples (see text for further details).

detection limit and the U and Th composition, a maximum age for monazite growth can be estimated at 90–100 Ma [following the approach of Montel *et al.* (2000); see Supplementary Data S1].

Geochronological results

In all investigated samples, allanite exhibits high Th/U ratios and a higher variability of Th/Pb relative to U/Pb. Therefore, the Th-isochron approach was favored to constrain the final age of a given population using the slope of the regression line and to retrieve the initial Pb composition ^{208}Pb/^{206}Pbc (as suggested by Gregory *et al.*, 2007; Janots & Rubatto, 2014). The resulting uncertainties in common lead composition (f_{206}) estimated by the isochron method were propagated through the age calculation procedure using a Monte-Carlo technique (Burn *et al.*, 2017).

Dating results are summarized in Fig. 10. In sample w13-4, the Th-isochron defined by 15 analyses (corresponding to 10 analyzed grains) yielded an age of 179·8 ± 8·7 Ma (2σ). In sample w13-3, the slope of the isochron (25 allanites for 10 analyzed grains both in the matrix and as inclusions in garnet) yielded an older age of 203·2 ± 4·2 Ma (2σ). An age of 182·7 ± 5·8 Ma was calculated for allanite from sample w13-2 (10 analyzed grains). In contrast, two distinct groups of allanite were observed in the Th-isochron diagram for sample w13-1. The first one (group 1, Gr1) has a low Al content of 2·08–2·18 a.p.f.u. (measured by LA-ICP-MS), consistent with the Al concentrations determined by EPMA for Aln, and an age of 200·3 ± 7·3 Ma (Fig. 10d and e). The second group (Gr2 in Fig. 10e) shows a higher Al content (2·19–2·29 a.p.f.u.), corresponding to EPMA values for Ep1, and yielded a younger age of 180·3 ± 13·5 Ma (Fig. 10d).

DISCUSSION

Critical evaluation of thermobarometric results

The results from thermodynamic modeling and Ti-in-biotite thermometry show that all studied samples experienced peak metamorphic conditions (T_{max}) between 560 and 600°C. Sample w13-5 is the one that best preserves the prograde to peak path from 7·5 kbar,

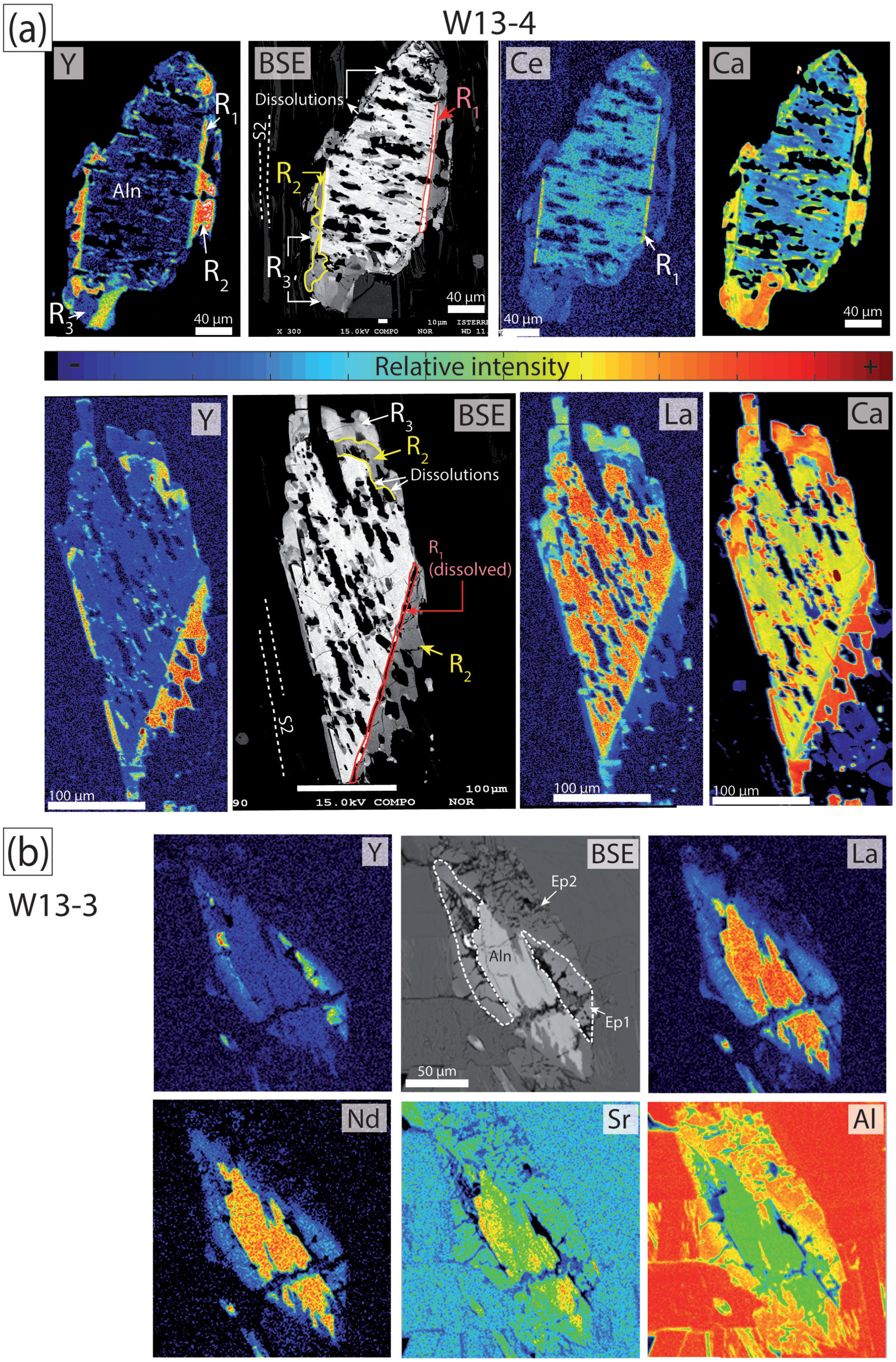

Fig. 9. EPMA maps of two representative allanite grains in samples w13-4 (a) and w13-3 (b).

530°C to 10 kbar, 597°C. In sample w13-4, *P* cannot be constrained using garnet. However, the absence of staurolite, the volume fractions of biotite and garnet observed in the thin section, and the measured Si content of biotite and Wm (Supplementary Data Fig. S1) are well reproduced along the same *P*–*T* path as retrieved for sample w13-5, suggesting similar *P* conditions of garnet growth (Fig. 7b). The difficulty in modeling the grossular fraction of garnet (and therefore the derived high uncertainty in *P*) can be related to the unusual Ca zoning revealed by EPMA. The highest Ca content might indeed be a minimal estimate if the very

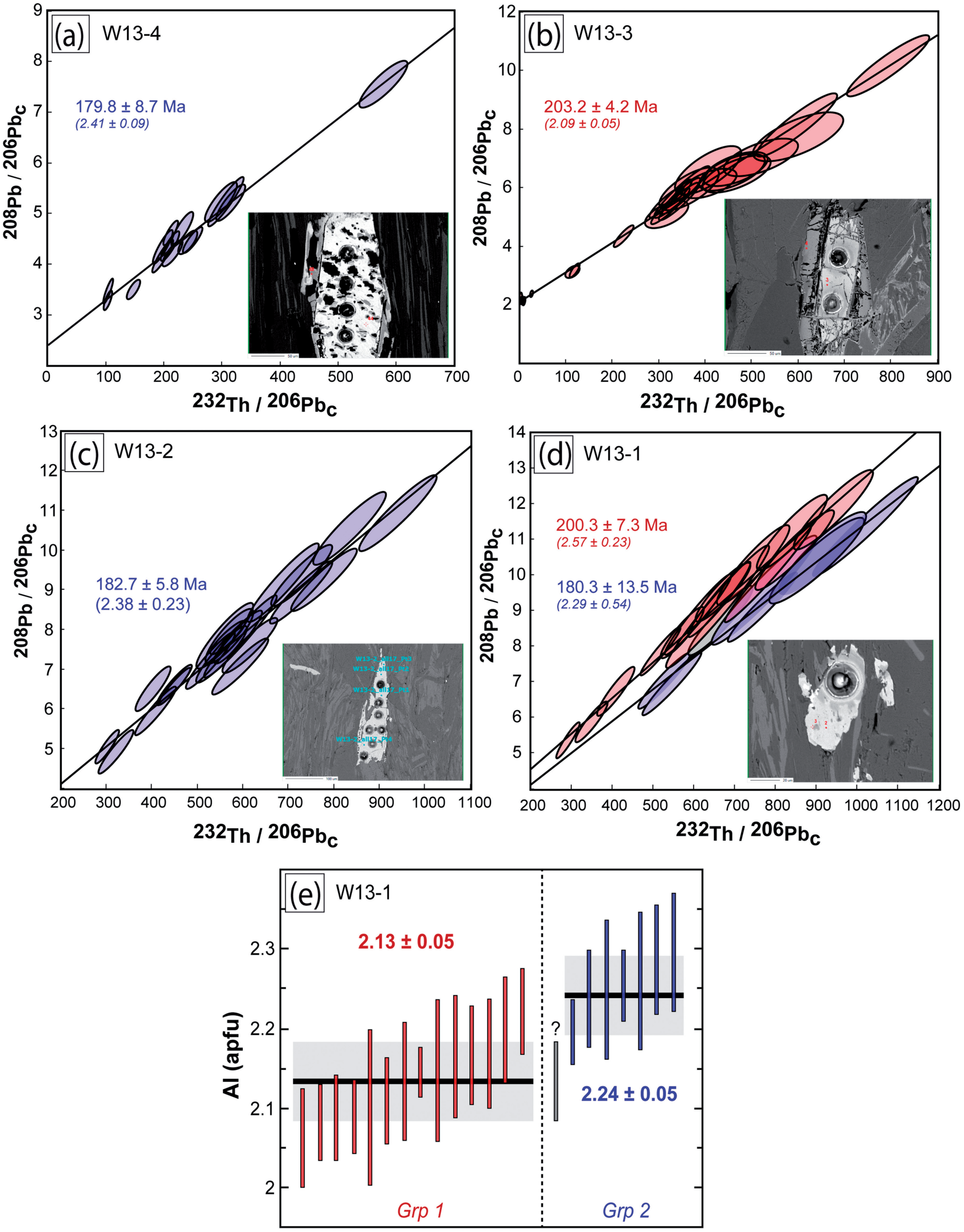

Fig. 10. Isochron $^{208}Pb/^{206}Pb_c$ vs $^{232}Th/^{206}Pb_c$ diagrams obtained for all dated samples (a–d) and Al (a.p.f.u.) content determined by LA-ICP-MS for the same volume of material of the two population of allanite in sample w13-1 (e) (see text for details). Each allanite analysis is represented by an ellipse. The calculated age is reported in color above the isochrons. Blue, age <200 Ma; red, age >200 Ma. Insets in isochron diagrams are representative allanite backscattered electron images showing the location of the laser spots (24 μm) used for dating. Numbers in brackets are the Pb isotopic ratios predicted by the 'global lead evolution model' of Stacey & Kramers (1975).

garnet core was missed, as the flat Mn and Fe zoning might indicate (Fig. 4b).

In sample w13-3, garnet grew at 560°C, 8 kbar, with a garnet reaction overstepping of ~100°C, quickly, as attested to by the absence of zoning in major elements and of earlier garnet relics. In this same sample, the Grt-bearing assemblage overprints the early S_1–S_2 cleavage that wraps the garnet and biotite in the other studied samples. Garnet in this sample may represent a prograde growth stage or the metamorphic peak, at slightly lower *P* than in sample w13-5. A small difference of *P* (considering the uncertainties) between samples w13-3 and w13-5 would be consistent with the small offset expected for the eastward prolongation of the WSW–ENE thrust fault bordering the Cambrian–Ordovician units into the Silurian sediments (Fig. 1b). This tectonic discontinuity may also have acted as a favored fluid path allowing the rapid development of the new mineral assemblage in sample w13-3 (e.g. Airaghi *et al.*, 2017*b*). It is of note that, whereas biotite precedes garnet growth in samples w13-5 and w13-3, biotite is syn- to post-garnet in sample w13-4, in good agreement with the petrological observations.

Temperature ranges estimated with the Ti-in biotite thermometry in 'fresh' garnet–biotite metapelites are in good agreement with prograde to peak temperatures calculated with the thermodynamic modeling approach. In the retrogressed samples w13-2 and w13-1, the Ti-in biotite thermometry and the RSCM thermometry reveal that the rocks also experienced amphibolite-facies conditions, as testified by the presence of biotite porphyroblast pseudomorphs (sample w13-1).

Timing and mechanisms of allanite growth

In all analyzed samples, matrix allanite and its rims are oriented in the main foliation. This strongly suggest that allanite grains are syn-S_2, although a partial rotation of the allanite grains during the incipient S_2-forming stage cannot be discarded, especially in samples w13-5 and w13-3. Microstructures suggest that allanite is pre-garnet and biotite (<520°C) in samples w13-5 and w13-3, but syn- to post-garnet (>520°C) and possibly syn-biotite in sample w13-4. Based on these observations and on compositional analyses, we attempt to correlate the timing and mechanisms of allanite growth to the composition and textures of the other minerals. We especially characterize the partitioning of Y between garnet and allanite–epidote, which has already been used as a good proxy for evaluating the growth conditions of other accessory minerals, such as monazite, xenotime, apatite, and zircon (e.g. Bea & Montero, 1999; Rubatto *et al.*, 2001; Rubatto, 2002, 2017; Spear & Pyle, 2002; Pyle & Spear, 2003; Kohn & Malloy, 2004; Kohn *et al.*, 2004, 2005; Yang & Pattison, 2006; Gieré *et al.*, 2011; Regis *et al.*, 2016).

Pre-garnet allanite growth in garnet–biotite metapelites

In samples w13-3 and w13-5, allanite, as inclusions in garnet and in the matrix, exhibits the same number of epidote rims (Ep1 and Ep2), suggesting that they are prograde features preceding garnet growth, in agreement with observations by Janots *et al.* (2008) and Kim *et al.* (2009). It should be noted that allanite is observed as inclusions in garnet only in samples w13-5 and w13-3, but this preservation cannot only be due to the high volume-fraction of garnet in these samples. Garnet is indeed significantly present also in sample w13-4 (~5 vol. %) where grains are even more randomly distributed (Fig. 2). Prograde growth is also supported by the Y content in garnet, which is close to, or below, the EPMA detection limit. Owing to the significant REE concentration in the bulk-rock w13-3, the low Y content in garnet indicates that Y (and heavy REE; HREE) is mainly distributed in Aln and Ep1. In this case, garnet growing after allanite–epidote does not equilibrate with respect to the Y and HREE, as they are sequestered in allanite and epidote rims and remain isolated from the reactive bulk composition (Fig. 11a).

The prograde allanite-producing reactions remain difficult to assess. The presence of apatite as inclusions in garnet and in the matrix might suggest that allanite formed from the breakdown of monazite (± xenotime) present at low greenschist-facies metamorphic conditions [as proposed by Finger *et al.*, 1998; Wing *et al.*, 2003; Janots *et al.*, 2008; Fig. 11a (i)], but other REE sources cannot be ruled out. Microtextures and compositional analyses suggest that the partial dissolution of allanite provided the REE that were incorporated in the Ep1 and Ep2 rims [Fig. 11a (ii)]. The Y enrichment of Ep1, however, cannot be explained only with resorption of allanite, and requires the reaction of an Y-bearing additional phase, such as the remnant xenotime [Fig. 11a (ii)]. This is in line with the previously proposed breakdown reactions of monazite and xenotime as a mechanism to form allanite and Y-rich epidote rims (Janots *et al.*, 2008). The Ca necessary for epidote formation can be provided by the albitization of plagioclase. Garnet grew from Chl, Wm and Qz that formed the S_1–S_2 cleavages [Fig. 11a (iii)]. The CaO content of the bulk-rock of w13-3 (3·3 wt %; Table 2), is higher than in the other samples, and may have favored the prograde growth of allanite (see Engi, 2017, for a review). This is, however, not observed in sample w13-5, which exhibits a CaO content of only 0·46 wt %. Microstructures and model results suggest that allanite precedes garnet growth only in samples where biotite and garnet grew together or biotite slightly precedes the garnet growth (w13-5, w13-3). Wing *et al.* (2003) observed that in metapelites of Northern New England, USA, the appearance of allanite corresponds to the biotite-in isograd. We could therefore propose that also in our samples allanite formation is broadly simultaneous with the appearance of biotite, thus explaining the

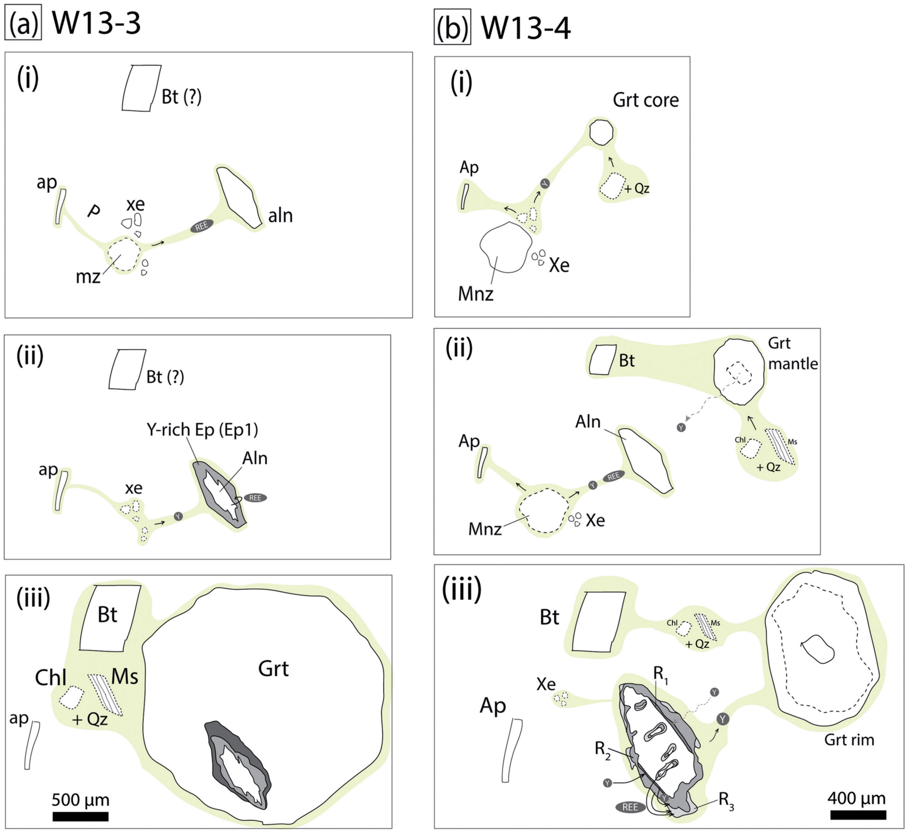

Fig. 11. Sketch illustrating possible allanite-forming reactions and the evolution of allanite rims in sample w13-3 (a) and w13-4 (b). It should be noted that allanite precedes the garnet growth in w13-3 and follows the appearance of garnet in w13-4 (see text for details). The size of allanite has been magnified 2× (a) and 5× (b) compared with the size observed in the thin section to allow the epidote rims to be distinguished.

differences in the timing of allanite growth (Fig. 11). The succession of (unbalanced) reactions can be thus considered as follows (Fig. 11a):

$$\mathrm{Mnz} + \mathrm{silicate} \rightarrow \mathrm{Aln}\ (\pm\mathrm{Ap}) + \mathrm{Biotite}\ (?)$$
$$\mathrm{Xe}\ (+\mathrm{Aln}) + \mathrm{silicate} \rightarrow \mathrm{Ep1}\ (\pm\mathrm{Ep2})$$
$$\mathrm{Chl} + \mathrm{Qz} + \mathrm{Plg} \rightarrow \mathrm{Ep2} + \mathrm{Ab}$$
$$\mathrm{Ms} + \mathrm{Chl} + \mathrm{Qz} \rightarrow \mathrm{Grt} + \mathrm{Bt}.$$

Syn- to post-garnet allanite growth in Grt–Bt metapelites

In sample w13-4, allanite is observed only in the matrix, suggesting that it postdates the garnet growth. The post-garnet growth of allanite is also supported by the Y content in garnet, which is higher than in samples w13-3 and w13-5. Indeed, prior to allanite crystallization, garnet can represent the main host for Y (and HREE). The higher garnet modal abundance in sample w13-3 (>10 vol. %) relative to sample w13-4 (~5 vol. %) may account for a redistribution of Y in a larger volume of rock, but cannot account alone for the Y depletion of w13-3 garnet grains.

Sample w13-4 also exhibits complex garnet and allanite textures, with allanite showing evidence of resorption and replacement by epidote rims. Furthermore, the discontinuous Y zoning in garnet is not compatible with a Rayleigh fractionation model (Otamendi *et al.*, 2002), supporting a supply of Y from the breakdown or resorption of Y-bearing accessory phases during garnet growth [Fig. 11b (i) and (ii)]. Prior to allanite formation, xenotime might be evoked as a source of Y [as proposed by Spear & Pyle, 2002; Pyle & Spear, 2003; Yang & Rivers, 2003; Fig. 11a (i)]. The Y content in the garnet mantle then decreases, as Y is sequestrated from the reactive volume by the growth of allanite [Fig. 10b (ii)]. The competition between the slow diffusion of Y and the relatively fast garnet-mantle growth rate required to explain the trapping of inclusions (Yang & Rivers (2003)) might also partially account for the Y depletion in garnet mantles. Furthermore, both garnet and allanite rims show features that suggest fluid-assisted reactions. Allanite and its rims are partially dissolved and contain quartz and epidote inclusions (T2 and T3) with epidote compositions similar to those found in the rims (R2 and R3, Fig. 9a and Table 4). Inclusion trails have different orientations depending on the allanite section, attesting that they are not relics of an early foliation (S_1). Furthermore, they crosscut not only the allanite but also the epidote rims, showing that they grew later. It is therefore proposed that these are secondary epidote inclusions, caused by dissolution and replacement of the primary allanite. Similar textures with secondary inclusions within a primary accessory phase were observed in experimentally altered monazite (Budzyń & Kozub-Budzyń, 2015; Grand d'Homme et al., 2016*b*). To our knowledge, this process has rarely been described in natural samples. Secondary inclusions are interpreted to result from precipitation in pores caused by the dissolution along crystallographic planes or channelized pathways (e.g. nanocracks) created during replacement by interfacially coupled dissolution–precipitation (Putnis, 2009; Putnis & John, 2010; Grand d'Homme et al., 2016*b*). Allanite resorption could account for the REE content of the allanite rims, but cannot explain the Y enrichment. R1 and R2 may therefore have formed from the concomitant partial dissolution of allanite and another Y source that could be represented by a REE-bearing phase [e.g. residual xenotime; Fig. 11b (iii); see also Regis *et al.*, 2012] or by the reactive fluid. The Y enrichment of garnet rims and the REE enrichment in R3 may witness the partial dissolution of allanite, R1 and R2 [Fig. 11b (iii)]. The growth of R3 (REE-rich clinozoisite composition) may contribute to the decrease of the Ca content in the garnet rims. A minor resorption of garnet core and mantle could have equally participated in the mobilization of Y, as indicated by the garnet textural zoning (Fig. 4b). To summarize, the successive (unbalanced) reactions of growth and resorption of allanite and its rims in sample w13-4 can be written as

$$\begin{aligned}&\mathrm{Xe}\ (?) + \mathrm{Chl} + \mathrm{Qz} \rightarrow \mathrm{Grt\ core} + \mathrm{Ap} +\ \mathrm{H_2O}\\&\mathrm{Mnz}\ (?) + \mathrm{Chl} + \mathrm{Qz} + \mathrm{Ms}\ (\pm \mathrm{Grt\ core}) \rightarrow \mathrm{Grt\ mantle}\\&\ + \mathrm{Bt} + \mathrm{Aln}\ (\pm \mathrm{Ap}) +\ \mathrm{H_2O}\\&\mathrm{Aln} + (\pm \mathrm{Xe}) + \mathrm{Grt\ mantle} \rightarrow \mathrm{R1} + \mathrm{R2} \pm \mathrm{R3} + \mathrm{Grt\ rims}.\end{aligned}$$

Allanite replacement in retrogressed samples

For samples w13-2 and w13-1, located close to or within the WSZ, strong evidence of the greenschist overprint is found owing to deformation (up to mylonitization in w13-1) and fluid-assisted reaction (e.g. Bt alteration and pseudomorphs). This retrogression leads to a decrease of allanite grain size by fragmentation and its alteration to Mnz at the rim, along cracks and as secondary inclusions (see previous section). However, primary allanite shows no significant elemental or isotopic changes. Allanite grains have compositions similar to those in samples w13-3, w13-4 and w13-5 and exhibit ages in the same interval, indicating that they grew during the same metamorphic event. Allanite displays few relics of epidote rims, suggesting that they preferentially reacted during retrogression. Because no monazite was observed in fresh Grt–Bt metapelites, monazite is interpreted to have formed during the greenschist overprint in the most retrogressed samples. In the study by Cenki-Tok *et al.* (2011), Permian allanite preservation in Alpine mylonite was attributed to the mechanical and chemical effects of shielding provided by epidote rims around allanite during mylonitization. In our samples, such a process may explain the allanite preservation and the disappearance of allanite rims in deformed and retrogressed samples, according the unbalanced reaction

$$\mathrm{Aln} + \mathrm{Ep\ \ rim} + \mathrm{Fluid} \rightarrow \mathrm{Mnz} + \mathrm{Wm} + \mathrm{Qtz}.$$

Critical evaluation of the geochronological data

Our thermometric estimates show that allanite formed below the closure *T* for Pb diffusion (>700–750°C; Rubatto *et al.*, 2001; Gregory *et al.*, 2012; Engi, 2017). Therefore, allanite is expected to record growth ages. To check the quality of our age results we tested if the application of a common Pb correction based on the isotopic ratio predicted by the 'global lead evolution model' of Stacey & Kramers (1975) still defined one single age group as the isochron approach indicates. This was verified for allanite of samples w13-2, w13-3 and w13-4. In sample w13-1, two age groups were observed with both approaches (Gr1 and Gr2 in Fig. 10d and e).

Although in the most retrogressed sample (w13-1), a large part of the original petrological information has been lost (e.g. Grt and Bt have disappeared), the ages of Gr1 (Al-poor; 200·3 ± 7·3 Ma) are close to the ages of allanite in sample w13-3, whereas ages of Gr2 (Al-depleted) are consistent with the allanite ages of sample w13-4 (Figs 10 and 12). A contribution of the muscovite surrounding the allanite grains (Al-enriched and Th–Pb depleted relative to allanite) cannot, however, be excluded, given the size of the laser spot (but will not affect the ages).

P–T–t paths, metamorphic rates and regional tectonic implications

The studied samples record a clockwise *P*–*T* path with peak conditions of up to ~600°C, 10 kbar (suggesting a thickening of the metasedimentary pile up to ~30 km; Fig. 12). These results are in very good agreement with the *T* range predicted for allanite stability (Janots *et al.*, 2007) and with the *P*–*T* estimates of Robert *et al.* (2010*b*) and Airaghi *et al.* (2017*b*) ~40 km to the NE (Tonghua area, Fig. 1a) and in the central Longmen Shan. Microtextural observations suggest that syn-S_2 allanite in sample w13-3 formed during the prograde path (to *P* peak), whereas post-garnet allanite in sample w13-4 is likely to indicate the timing of the temperature peak. It is therefore possible to define for the studied samples (1) a prograde path from 520 to 597°C, at *c.* 200 Ma, related to the thickening of Songpan Ganze sediments in the accretionary prism, which can be linked to the closure of the Paleotethys, and (2) a metamorphic peak, and thermal relaxation and exhumation at *c.* 180 Ma (Fig. 12). The timing of these stages is consistent with the timing of the two-step amphibolite-facies metamorphism (at *c.* 220–200 and *c.* 180 Ma) revealed by the

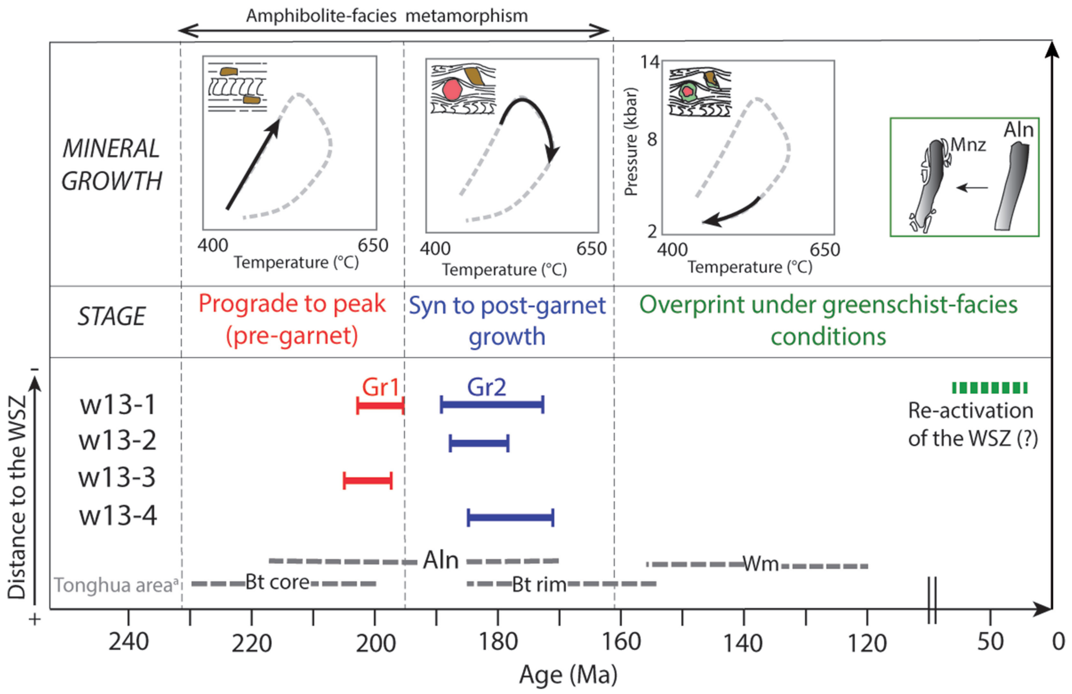

Fig. 12. Summary of the ages obtained in this study by U–Th/Pb allanite dating (bold lines) and their relation to petrological and microstructural events. Dashed grey line indicate ages reported in literature for the Tonghua area (Airaghi *et al.*, 2018*a*).

Table 5: Representative chemical analyses of monazite in sample w13-1

Oxide	d.l.	Mnz1	Mnz2	Mnz3	Mnz4	Mnz5	Mnz6	Mnz7	Mnz8	Mnz9	Mnz10	Mnz11	Mnz12	Mnz13
P_2O_5	257	29·739	30·124	29·562	30·179	30·242	30·361	29·999	29·191	30·158	30·140	29·678	30·058	29·878
As_2O_5	149	0·165	0·168	0·158	0·203	0·147	0·191	0·184	0·118	0·187	0·183	0·158	0·170	0·109
ThO_2	138	2·287	0·694	3·864	0·372	0·132	0·403	0·501	0·235	1·089	0·407	3·153	2·763	0·182
UO_2	141	0·107	0·049	0·093	0·075	0·039	0·043	0·056	0·057	0·026	0·031	0·052	0·080	0·116
Al_2O_3	—	0·030	0·123	0·028	0·027	0·068	0·000	0·089	0·032	0·000	0·000	1·488	0·882	0·871
Y_2O_3	231	0·366	0·384	0·367	0·584	0·351	0·302	0·450	0·413	0·391	0·325	0·306	0·503	0·532
La_2O_3	—	16·369	16·288	15·081	15·343	17·103	16·903	15·904	15·968	16·115	16·794	15·548	16·198	15·951
Ce_2O_3	—	31·199	32·205	29·472	31·916	32·207	32·444	31·762	31·006	31·308	32·305	31·315	31·147	31·768
Pr_2O_3	—	3·006	3·061	2·860	3·165	3·033	3·061	3·076	2·893	3·018	2·989	2·963	2·838	3·009
Nd_2O_3	—	12·337	13·289	11·167	13·711	12·242	12·534	12·432	11·874	12·276	12·301	12·405	12·050	12·944
Sm_2O_3	—	1·471	1·670	1·515	2·090	1·609	1·687	1·567	1·685	1·638	1·397	1·476	1·527	1·666
Gd_2O_3	—	1·032	1·048	0·867	1·330	1·020	0·990	1·235	1·011	0·947	1·014	0·853	1·075	1·226
Dy_2O_3	—	0·000	0·000	0·000	0·000	0·000	0·000	0·000	0·000	0·000	0·000	0·000	0·000	0·000
CaO	106	0·269	0·143	0·332	0·070	0·085	0·087	0·107	0·097	0·204	0·076	0·274	0·358	0·067
PbO	130	0·000	0·000	0·006	0·006	0·009	0·000	0·000	0·004	0·000	0·000	0·008	0·000	0·006
Total		98·904	99·386	95·708	99·208	98·414	99·091	97·607	95·940	97·446	98·057	100·016	—	99·556
Cations														
P		0·994	1·000	1·019	1·005	1·010	1·011	1·009	0·988	1·018	1·013	0·967	0·980	0·968
As		0·003	0·003	0·003	0·004	0·003	0·004	0·004	0·002	0·004	0·004	0·003	0·003	0·002
Th		0·021	0·006	0·036	0·003	0·001	0·004	0·005	0·002	0·010	0·004	0·028	0·024	0·002
U		0·001	0·000	0·001	0·001	0·000	0·000	0·000	0·001	0·000	0·000	0·000	0·001	0·001
Al		0·001	0·006	0·001	0·001	0·003	0·000	0·004	0·002	0·000	0·000	0·067	0·040	0·039
Y		0·008	0·008	0·008	0·012	0·007	0·006	0·010	0·009	0·008	0·007	0·006	0·010	0·011
La		0·238	0·236	0·226	0·223	0·249	0·245	0·233	0·236	0·237	0·246	0·221	0·230	0·225
Ce		0·451	0·463	0·439	0·459	0·465	0·467	0·462	0·454	0·457	0·470	0·441	0·439	0·445
Pr		0·043	0·044	0·042	0·045	0·044	0·044	0·045	0·042	0·044	0·043	0·042	0·040	0·042
Nd		0·174	0·186	0·162	0·193	0·173	0·176	0·176	0·170	0·175	0·174	0·170	0·166	0·177
Sm		0·020	0·023	0·021	0·028	0·022	0·023	0·021	0·023	0·023	0·019	0·020	0·020	0·022
Gd		0·014	0·014	0·012	0·017	0·013	0·013	0·016	0·013	0·013	0·013	0·011	0·014	0·016
Dy		0·000	0·000	0·000	0·000	0·000	0·000	0·000	0·000	0·000	0·000	0·000	0·000	0·000
Ca		0·011	0·006	0·014	0·003	0·004	0·004	0·005	0·004	0·009	0·003	0·011	0·015	0·003
Pb		0·000	0·000	0·000	0·000	0·000	0·000	0·000	0·000	0·000	0·000	0·000	0·000	0·000
ΣREE		0·948	0·972	0·911	0·978	0·973	0·974	0·963	0·947	0·956	0·972	0·910	0·919	0·938
LREE		0·773	0·763	0·777	0·744	0·779	0·776	0·768	0·773	0·772	0·780	0·772	0·771	0·760
MREE		0·219	0·229	0·214	0·244	0·214	0·217	0·222	0·218	0·220	0·213	0·221	0·217	0·229
Y		0·008	0·008	0·009	0·012	0·008	0·006	0·010	0·009	0·009	0·007	0·007	0·011	0·012

Detection limits (d.l.) are expressed in ppm.

$^{40}Ar/^{39}Ar$ ages of syn- to post-D_2 biotite grains obtained for samples located ∼40 km northeastward in an equivalent structural position (Airaghi *et al.*, 2018*a*; dashed lines in Fig. 12). This strengthens the interpretation that allanite growth is coeval with the D_2-deformation stage and shows that in the central Longmen Shan, far from the major fault zone, biotite retains Ar-Ar crystallization ages (Airaghi *et al.*, 2018*a*) at $T > 550°C$. Geochronological results are also in line with the monazite and zircon U–Pb ages obtained by Huang *et al.* (2003*b*), Weller *et al.* (2013) and Jolivet *et al.* (2015) for the onset of the Barrovian metamorphism in the Danba area (∼150 km to the SE; Fig. 1a). Hence, in the Longmen Shan, allanite records in its texture and composition the two-stage amphibolite-facies metamorphism revealed by petrology (Airaghi *et al.*, 2017*b*). Allanite formation during prograde up to peak metamorphism covers a range of *c.* 20 Myr (Fig. 12), consistent with the interval of granite emplacement in the SPG block (Roger *et al.*, 2004; de Sigoyer *et al.*, 2014).

The similarity between the peak-*T* conditions and the allanite ages recorded in sample w13-1—located in Devonian units and close to a major tectonic lineament—and those recorded in the fresh Silurian metapelites far from the fault indicates that all these samples underwent a similar amphibolite-facies metamorphism. The increasing greenschist overprint (as low as 3 ± 1 kbar, 350–400°C) approaching the Wenchuan Shear Zone (samples w13-2 and w13-1) supports the hypothesis that faults act as zone of localizing deformation and favored fluid paths, triggering mineral re-equilibration. The *P*–*T* estimates for the greenschist-facies overprint are consistent with the 400–450°C proposed for the breakdown of allanite into monazite during greenschist retrogression (Bollinger & Janots, 2006; Janots *et al.*, 2008) and with the temperature estimated for the greenschist-facies assemblage in the metapelites of the Tonghua area (Airaghi *et al.*, 2017*b*; Fig. 1). Based on the maximum age of the Pb-poor monazite replacing allanite during this retrogression, we propose a late reactivation of the WSZ at <90–100 Ma, immediately after the Cretaceous compressional reactivation of the belt recorded by $^{40}Ar/^{39}Ar$ muscovite ages in the Tonghua and Pengguan areas (Fig. 12; Airaghi *et al.*, 2017*a*, 2018*a*).

CONCLUSIONS

Five metapelites collected in the central Longmen Shan at a decreasing distance from the major WSZ experienced a consistent metamorphism under amphibolite-facies conditions (10–11 kbar, 560–600°C). In proximity to the WSZ, partial to complete greenschist overprinting occurred at 3–4 ± 1 kbar and 350–400°C.

Allanite in 'fresh' Grt–Bt metapelites exhibits a variable number of Y-enriched and Y-depleted epidote rims. In samples where both allanite and its rims are included in garnet, garnet is depleted in Y, suggesting that Y fractionated into allanite and was not remobilized during garnet growth. In samples where allanite is observed only in the matrix, garnet is Y-enriched, as Y was provided by the breakdown of Y-bearing accessory phases involving allanite growth or resorption reactions. The timing of allanite formation seems to correlate with the appearance of biotite in the stable mineral assemblage. Whole-rock composition and fluid availability during metamorphism are probable causes for textural differences amongst allanite in different samples, limiting its growth or resorption. The whole-rock composition may play an important role in determining the quantity of fluid released during the metamorphic reactions. Tectonic structures could also channelize fluids into the metamorphic rocks, triggering re-equilibration and mineral resorption.

Our petrochronological approach shows that detailed studies of the textures and composition of allanite can provide precious information on the timing of allanite growth. Pre-garnet allanite yields Th/Pb ages of *c.* 200 Ma (timing of thickening of the Songpan–Ganze sediments during the closure of the Paleotethys), whereas post-garnet allanite exhibits ages of *c.* 180 Ma (timing of the peak-*T* and the beginning of exhumation). In the two more deformed and retrogressed samples, allanite still preserves the same chemical and isotopic signatures as in fresh garnet–biotite metapelites, but it is partially replaced along its rims by monazite with ages <90–100 Ma, pointing to a late activation of the WSZ.

ACKNOWLEDGEMENTS

We thank John Brady, Somnath Dasgupta and the two anonymous reviewers for their constructive criticism, and acknowledge the very helpful suggestions for improvement by the editor Reto Gieré. We also thank Stéphane Guillot for constructive discussions, and Dr Tan Xibin (China Earthquake Administration) and the students from Chengdu University for their logistical support in the field.

FUNDING

The project was made possible by the financial support of Agence Nationale de la Recherche (ANR) AA-PJCJC SIMI5-6 LONGRIBA, ANR-13-BS06-012-01 DSP-Tibet, ANR-12-JS06-0001-01 MONA, the INSU-CNRS and LabEx 'OSUG@2020' (ANR).

SUPPLEMENTARY DATA

Supplementary data for this paper are available at *Journal of Petrology* online.

REFERENCES

Airaghi, L., de Sigoyer, J., Guillot, S., Robert, A., Warren, C. J. & Deldicque, D. (2018b). The Mesozoic Along-Strike Tectonometamorphic Segmentation of Longmen Shan (Eastern Tibetan Plateau). Tectonics, in press.

Airaghi, L., de Sigoyer, J., Lanari, P., Guillot, S., Vidal, O., Monié, P., Sautter, B. & Tan, X. (2017a). Total exhumation across the Beichuan fault in the Longmen Shan (eastern Tibetan plateau, China): constraints from petrology and thermobarometry. *Journal of Asian Earth Sciences* **140**, 108–121.

Airaghi, L., Lanari, P., de Sigoyer, J. & Guillot, S. (2017b). Microstructural vs compositional preservation and pseudomorphic replacement of muscovite in deformed metapelites from the Longmen Shan (Sichuan, China). *Lithos* **282–283**, 260–280.

Airaghi, L., Warren, C. J., de Sigoyer, J., Lanari, P. & Magnin, V. (2018a). Influence of dissolution/reprecipitation reactions on metamorphic greenschist to amphibolite-facies mica ^{40}Ar/^{39}Ar ages in the Longmen Shan. *Journal of Metamorphic Geology* **36**, 933–958.

Arne, D., Worley, B., Wilson, C., Chen, S. F., Foster, D., Luo, Z. L., Liu, S. G. & Dirks, P. (1997). Differential exhumation in response to episodic thrusting along the eastern margin of the Tibetan Plateau. *Tectonophysics* **280**, 239–256.

Bea, F. & Montero, P. (1999). Behaviour of accessory phases and redistribution of Zr, REE, Y, Th and U during metamorphism and partial melting of metapelites in the lower crust: an example from the Kinzigite Formation of Ivrea–Verbano, NW Italy. *Geochimica et Cosmochimica Acta* **63**, 1133–1153.

Berger, A., Scherrer, N. C. & Bussy, F. (2005). Equilibration and disequilibration between monazite and garnet: indication from phase-composition and quantitative texture analysis. *Journal of Metamorphic Geology* **23**, 865–880.

Berman, R. G. (1988). Internally consistent thermodynamic data for minerals in the system $Na_2O–K_2O–CaO–MgO–FeO–Fe_2O_3–Al_2O_3–SiO_2–TiO_2–H_2O–CO_2$. *Journal of Petrology* **29**, 445–522.

Beyssac, O., Rouzaud, J. N., Goffé, B., Brunet, F. & Chopin, C. (2002). Graphitization in a high-pressure, low-temperatre metamorphic gradient: a Raman microspectroscopy and HRTEM study. *Contributions to Mineralogy and Petrology* **143**, 19–31.

Bollinger, L. & Janots, E. (2006). Evidence for Mio-Pliocene retrograde monazite in the Lesser Himalaya, far western Nepal. *European Journal of Mineralogy* **18**, 289–297.

Bucher, K. & Stober, I. (2002). Water-rock reaction experiments with Black Forest gneiss and granite. In: Stober I. & Bucher K. (eds) *Water-Rock Interaction. Water Science and Technology Library*. Volume **40**. Dordrecht: Springer.

Budzyń, B. & Kozub-Budzyń, G. A. (2015). The stability of xenotime in high Ca and Ca–Na systems, under experimental conditions of 250–350°C and 200–400 MPa: the implications for fluid-mediated low-temperature processes in granitic rocks. *Geological Quaterly* **59**, 316–324.

Burn, M., Lanari, P., Pettke, T. & Engi, M. (2017). Non matrix-matched standardization in LA-ICP-MS analysis: General approach, and application to allanite Th–U–Pb dating. *Journal of Analytical Atomic Spectrometry* **32**, 1359–1377.

Cenki-Tok, B., Oliot, E., Rubatto, D., Berger, A., Engi, M., Janots, E., Thomsen, T. B., Manzotti, P., Regis, D., Spandler, C. & Robyr, M. (2011). Preservation of Permian allanite within an Alpine eclogite facies shear zone at Mt Mucrone, Italy: mechanical and chemical behavior of allanite during mylonitisation. *Lithos* **125**, 40–50.

Chen, S. F. & Wilson, C. (1995). Emplacement of the Longmen Shan Thrust–Nappe Belt along the eastern margin of the Tibetan Plateau. *Journal of Structural Geology* **18**, 413–430.

Corrie, S. L. & Kohn, M. J. (2008). Trace-element distribution in silicates during prograde metamorphic reactions: implications for monazite formation. *Journal of Metamorphic Geology* **26**, 451–464.

Cossette, E., Schneider, D. A., Warren, C. J. & Grasemann, B. (2015). Lithological, rheological, and fluid infiltration control on ^{40}Ar/^{39}Ar ages in polydeformed rocks from the West Cycladic detachment system, Greece. *Lithosphere* **7**, 189–205.

de Capitani, C. & Brown, T. H. (1987). The computation of chemical equilibrium in complex systems containing non-ideal solutions. *Geochimica et Cosmochimica Acta* **51**, 2639–2652.

de Capitani, C. & Petrakakis, K. (2010). The computation of equilibrium assemblage diagrams with Theriak/Domino software. *American Mineralogist* **95**, 1006–1016.

de Sigoyer, J., Vanderhaeghe, O., Duchene, S. & Billerot, A. (2014). Generation and emplacement of Triassic granitoids within the Sonpan Ganze accretionary orogenic wedge in a context of slab retreat accommodated by tear faulting, Eastern Tibetan Plateau, China. *Journal of Asian Earth Sciences* **88**, 192–216.

Diener, J. F. A. & Powell, R. (2010). Influence of ferric iron on the stability of mineral assemblages. *Journal of Metamorphic Geology* **28**, 599–613.

Dirks, P., Wilson, C. J. L., Chen, S., Luo, Z. L. & Liu, S. (1994). Tectonic evolution of the NE margin of the Tibetan Plateau; evidence from central Longmen Mountains, Sichuan Province, China. *Journal of Southeast Asian Earth Sciences* **9**, 181–192.

Dubacq, B., Vidal, O. & De Andrade, V. (2010). Dehydration of dioctahedral aluminous phyllosilicates: thermodynamic modelling and implications for thermobarometric estimates. *Contributions to Mineralogy and Petrology* **159**, 159–174.

Engi, M. (2017). Petrochronology based on REE-minerals: monazite, allanite, xenotime, apatite. In: Kohn, M. J., Engi, M.& Lanari, P. (eds) *Petrochronology: Methods and Applications. Mineralogical Society of America and Geochemical Society, Reviews in Mineralogy and Geochemistry* **83**, 365–418.

Finger, F., Broska, I., Roberts, M. & Schermaier, A. (1998). Replacement of primary monazite by apatite–allanite–epidote rims in an amphibolite facies granite gneiss from the eastern Alps. *American Mineralogist* **83**, 248–258.

Finger, F., Krenn, E., Schulz, B., Harlov, D. & Schiller, D. (2016). 'Satellite monazites' in polymetamorphic basement rocks of the Alps: their origin and petrological significance. *American Mineralogist* **101**, 1094–1103.

Gieré, R. & Sorensen, S. S. (2004). Allanite and other REE-rich epidote-group minerals. In: Liebscher, A.& Franz, G. (eds) *Epidotes. Mineralogical Society of America and Geochemical Society, Reviews in Mineralogy and Geochemistry* **56**, 431–493.

Gieré, R., Rumble, D., Günther, D., Connolly, J. & Caddick, M. J. (2011). Correlation of growth and breakdown of major and accessory minerals in metapelites from Campolungo, central Alps. *Journal of Petrology* **52**, 2293–2334.

Giuntoli, F., Lanari, P., Burn, M., Kunz, B. E. & Engi, M. (2018). Deeply subducted continental fragments—part 2: insight from petrochronology in the central Sesia Zone (western Italian Alps). *Solid Earth* **9**, 191–222.

Godard, V., Pik, R., Lav, J., Cattin, R., Tibari, B.,D.Sigoyer, J.Pubellier, M. & Zhu, J. (2009). Late Cenozoic evolution of the central Longmen Shan, eastern Tibet: Insight from (U–Th)/He thermochronometry. *Tectonics* **28**, TC5009.

Goswami-Banerjee, S. & Robyr, M. (2015). Pressure and temperature conditions for crystallization of metamorphic allanite and monazite in metapelites: a case study from the Miyar

Valley (high Himalayan Crystalline of Zanskar, NW India). *Journal of Metamorphic Geology* **33**, 535–556.

Grand d'Homme, A., Janots, E., Seydoux-Guillaume, A.-M., Guillaume, D., Bosse, V. & Magnin, V. (2016). Partial resetting of the U–Th–Pb systems in experimentally altered monazite: nanoscale evidence of incomplete replacement. *Geology* **44**, 431–434.

Gregory, C. J., Rubatto, D., Allen, C. M., Williams, I. S., Hermann, J. & Ireland, T. (2007). Allanite micro-geochronology: a LA-ICPMS and SHRIMP U–Th–Pb study. *Chemical Geology* **245**, 162–182.

Gregory, C. J., Rubatto, D., Hermann, J., Berger, A. & Engi, M. (2012). Allanite behavior during incipient melting in the southern Central Alps. *Geochimica et Cosmochimica Acta* **84**, 433–458.

Harrowfield, M. J. & Wilson, C. J. L. (2005). Indosinian deformation of the Songpan Garzê Fold Belt, northeast Tibetan Plateau. *Journal of Structural Geology* **27**, 101–117.

Henry, D. J., Guidotti, C. V. & Thomson, J. A. (2005). The Ti-saturation surface for low-to-medium pressure metapelitic biotites: implications for geothermometry and Ti-substitution mechanisms. *American Mineralogist* **90**, 316–328.

Holland, T. J. B. & Powell, R. (1998). An internally consistent thermodynamic data set for phases of petrological interest. *Journal of Metamorphic Geology* **16**, 309–343.

Huang, M., Maas, R., Buick, I. S. & Williams, I. S. (2003). Crustal response to continental collision between the Tibet, Indian, South China and North China Blocks: geochronological constraints from the Songpan-Garzê Orogenic Belt, western China. *Journal of Metamorphic Geology* **21**, 223–240.

Indares, A. (1995). Metamorphic interpretation of high-pressure–temperature metapelites with preserved growth zoning in garnet, eastern Grenville Province, Canadian Shield. *Journal of Metamorphic Geology* **13**, 476–486.

Janots, E. & Rubatto, D. (2014). U–Th–Pb dating of collision in the external Alpine domains (Urseren zone, Switzerland) using low temperature allanite and monazite. *Lithos* **184–187**, 155–166.

Janots, E., Negro, F., Brunet, F., Goffé, B., Engi, M. & Bouybaouène, M. L. (2006). Evolution of the REE mineralogy in HP–LT metapelites of the Sebtide complex, Rif, Morocco: monazite stability and geochronology. *Lithos* **87**, 214–234.

Janots, E., Brunet, F., Goffé, B., Poinssot, C., Burchard, M. & Cemič, L. (2007). Thermochemistry of monazite-(La) and dissakisite-(La): implications for monazite and allanite stability in metapelites. *Contributions to Mineralogy and Petrology* **154**, 1–14.

Janots, E., Engi, M., Berger, A., Allaz, J., Schwarz, J.-O. & Spandler, C. (2008). Prograde metamorphic sequence of REE minerals in pelitic rocks of the Central Alps: implications for allanite–monazite–xenotime phase relations from 250 to 610°C. *Journal of Metamorphic Geology* **26**, 509–526.

Janots, E., Engi, M., Rubatto, D., Berger, A., Gregory, C. & Rahn, M. (2009). Metamorphic rates in collisional orogeny from *in situ* allanite and monazite dating. *Geology* **37**, 11–14.

Janots, E., Berger, A. & Engi, M. (2011). Physico-chemical control on the REE-mineralogy in chloritoid-grade metasediments from a single outcrop (Central Alps, Switzerland). *Lithos* **121**, 1–11.

Jolivet, M., Roger, F., Xu, Z. Q., Paquette, J.-L. & Cao, H. (2015). Mesozoic–Cenozoic evolution of the Danba dome (Songpan Garzê, East Tibet) as inferred from LA-ICPMS U–Pb and fission-track data. *Journal of Asian Earth Sciences* **102**, 180–204.

Kim, Y., Yi, K. & Cho, M. (2009). Parageneses and Th–U distribution among allanite, monazite, and xenotime in Barrovian metapelites, Imjingang belt, central Korea. *American Mineralogist* **94**, 430–438.

Kirby, E., Reiners, P., Krol, M., Hodges, K., Whipple, K., Farley, K., Tang, W. & Chen, Z. (2002). Late Cenozoic uplift and landscape evolution along the eastern margin of the Tibetan Plateau: Inferences from ^{40}Ar/^{39}Ar and (U–Th)/He thermochronology. *Tectonics* **21**, 1001.

Kohn, M. J. (2008). *P–T–t* data from central Nepal support critical taper and repudiate large-scale channel flow of the Greater Himalayan Sequence. *Geological Society of America Bulletin* **120**, 259–273.

Kohn, M. J. & Malloy, M. A. (2004). Formation of monazite via prograde metamorphic reactions among common silicates: implications for age determinations. *Geochimica et Cosmochimica Acta* **68**, 101–113.

Kohn, M. J., Wieland, M. S., Parkinson, C. D. & Upreti, B. N. (2004). Miocene faulting at plate tectonic velocity in the Himalaya of central Nepal. *Earth and Planetary Science Letters* **228**, 229–310.

Kohn, M. J., Wieland, M. S., Parkinson, C. D. & Upreti, B. N. (2005). Five generations of monazite in Langtang gneisses: implications for chronology of the Himalaya metamorphic core. *Journal of Metamorphic Geology* **23**, 399–406.

Lanari, P. & Engi, M. (2017). Local bulk composition effects on mineral assemblages. In: Burns, P. C. & Finch, R. (eds) *Uranium: Mineralogy, Geochemistry and the Environment. Mineralogical Society of America and Geochemical Society, Reviews in Mineralogy and Geochemistry* **38**, 55–102.

Lanari, P., Guillot, S., Schwartz, S., Vidal, O., Tricart, P., Riel, N. & Beyssac, O. (2012). Diachronous evolution of the alpine continental subduction wedge: Evidence from *P–T* estimates in the Briançonnais Zone houillère (France—Western Alps). *Journal of Geodynamics* **56–57**, 39–54.

Lanari, P., Riel, N., Guillot, S., Vidal, O., Schwartz, S., Pêcher, A. & Hattori, K. H. (2013). Deciphering high-pressure metamorphism in collisional context using microprobe mapping methods: Application to the Stak eclogitic massif (northwest Himalaya). *Geology* **41**, 111–114.

Lanari, P., Vidal, O., De Andrade, V., Dubacq, B., Lewin, E., Grosch, E. & Schwartz, S. (2014). XMapTools: a MATLAB-based program for electron microprobe X-ray image processing and geothermobarometry. *Computers and Geosciences* **62**, 227–240.

Lanari, P., Vho, A., Bovay, T., Airaghi, L. & Centrella, S. (2018). Quantitative compositional mapping of mineral phases by electron probe micro-analyser. In: Ferrero, S., Lanari, P., Goncalves, P. & Grosch, E. G. (eds) *Metamorphic Geology: Microscale to Mountain Belts.* Geological Society, London, Special Publications **478** (in press).

Li, S., Currie, B. S., Rowley, D. B. & Ingalls, M. (2015). Cenozoic paleoaltimetry of the SE margin of the Tibetan plateau: constraints on the tectonic evolution of the region. *Earth and Planetary Science Letters* **432**, 415–424.

Li, Z.-W., Liu, S., Chen, H., Deng, B., Hou, M., Wu, W. & Cao, J. (2012). Spatial variation in Meso-Cenozoic exhumation history of the Longmen Shan thrust belt (eastern Tibetan Plateau) and adjacent western Sichuan basin: Constraints from fission track thermochronology. *Journal of Asian Earth Sciences* **47**, 185–203.

Loury, C., Rolland, Y., Cenki-Tok, B., Lanari, P. & Guillot, S. (2016). Late Paleozoic evolution of the South Tien Shan: insights from *P–T* estimates and allanite geochronology on retrogressed eclogites (Chatkal range, Kyrgyzstan). *Journal of Geodynamics* **96**, 62–80.

McDonald, S. C., Warren, C. J., Mark, D. F., Halton, A. M., Kelley, S. P. & Sherlock, S. C. (2016). Argon redistribution during a metamorphic cycle: consequences for determining cooling rates. *Chemical Geology* **224**, 182–197.

Montel, J.-M., Kornprobst, J. & Vielzeuf, D. (2000). Preservation of old U–Th–Pb ages in shielded monazite: example from the Beni Bousera Hercynian kinzigites (Morocco). *Journal of Metamorphic Geology* **18**, 335–342.

Otamendi, J. E., de la Rosa, J. D., Patiño Douce, A. E. & Castro, A. (2002). Rayleigh fractionation of heavy earths and yttrium during metamorphic garnet growth. *Geology* **30**, 159–162.

Powell, R. & Holland, T. J. B. (2008). On thermobarometry. *Journal of Metamorphic Geology* **26**, 155–179.

Putnis, A. (2009). Mineral replacement reactions. In: Oelkers, E. H. & Schott, J. (eds) *Thermodynamics and Kinetics of Water–Rock Interactions. Mineralogical Society of America and Geochemical Society, Reviews in Mineralogy and Geochemistry* **70**, 87–124.

Putnis, A. & John, T. (2010). Replacement processes in the Earth's crust. *Elements* **6**, 159–164.

Pyle, J. M. & Spear, F. S. (2003). Four generations of accessory-phase growth in low-pressure migmatites from SW New Hampshire. *American Mineralogist* **88**, 338–351.

Radulescu, I. G., Rubatto, D., Gregory, C. & Compagnoni, R. (2009). The age of HP metamorphism in the Gran Paradiso Massif, Western Alps: a petrological and geochronological study of 'silvery micaschists'. *Lithos* **110**, 95–108.

Regis, D., Cenki-Tok, B., Darling, J. & Engi, M. (2012). Redistribution of REE, Y, Th, and U at high pressure: allanite-forming reactions in impure meta-quartzites (Sesia Zone, Western Intalian Alps). *American Mineralogist* **97**, 315–328.

Regis, D., Warren, C. J., Mottram, C. M. & Roberts, M. W. (2016). Using monazite and zircon petrochronology to constrain the *P–T–t* evolution of the middle crust in the Bhutan Himalaya. *Journal of Metamorphic Geology* **34**, 617–639.

Richardson, N. J., Densmore, A. L., Seward, D., Fowler, A., Wipf, M., Ellis, M. A., Li, Y. & Zhang, Y. (2008). Extraordinary denudation in the Sichuan Basin: insights from low-temperature thermochronology adjacent to the eastern margin of the Tibetan Plateau. *Journal of Geophysical Research* **113**, B04409.

Robert, A., Pubellier, M., de Sigoyer, J., Vergne, J., Lahfid, A., Cattin, R., Findling, N. & Zhu, J. (2010). Structural and thermal characters of the Longmen Shan (Sichuan, China). *Tectonophysics* **491**, 165–173.

Roger, F., Malavieille, J., Leloup, P. H., Calassou, S. & Xu, Z. (2004). Timing of granite emplacement and cooling in the Songpan-Garzê fold belt (eastern Tibetan plateau) with tectonic implications. *Journal of Asian Earth Sciences* **22**, 465–481.

Roger, F., Jolivet, M. & Malavieille, J. (2010). The tectonic evolution of the Songpan-Garze (North Tibet) and adjacent areas from Proterozoic to Present: a synthesis. *Journal of Asian Earth Sciences* **39**, 254–269.

Rubatto, D. (2002). Zircon trace element geochemistry: partitioning with garnet and the link between U–Pb ages and metamorphism. *Geology* **184**, 123–138.

Rubatto, D. (2017). Zircon: the metamorphic mineral. In: Kohn, M. J., Engi, M. & Lanari, P. (eds) *Petrochronology: Methods and Applications. Mineralogical Society of America and Geochemical Society, Reviews in Mineralogy and Geochemistry* **83**, 261–295.

Rubatto, D., Williams, I. S. & Buick, I. S. (2001). Zircon and monazite response to prograde metamorphism in the Reynolds Range, central Australia. *Contributions to Mineralogy and Petrology* **140**, 458–468.

Rubatto, D., Regis, D., Hermann, J., Boston, K., Engi, M., Beltrando, M. & McAlpine, S. R. B. (2011). Yo-yo subduction recorded by accessory minerals in the Italian Western Alps. *Nature Geoscience* **4**, 338–342.

Shaw, D. M. (1956). Geochemistry of pelitic rocks. Part III. Major elements andgeneral geochemistry. *Geol SocAmBull* **67**, 919–934.

Sláma, J., Košler, J., Condon, D. J., Crowley, J. L., Gerdes, A., Hanchar, J. M., Horstwood, M. S. A., Morris, G. A., Nasdala, L., Norberg, N., Schaltegger, U., Schoene, B., Tubrett, M. N. & Whitehouse, M. J. (2008). Plešovice zircon—a new natural reference material for U–Pb and Hf isotopic microanalysis. *Chemical Geology* **249**, 1–35.

Smith, H. A. & Barreiro, B. (1990). Monazite U–Pb dating of staurolite grade metamorphism in pelitic schists. *Contributions to Mineralogy and Petrology* **105**, 602–615.

Sorensen, S. S. (1991). Petrogenic significance of zoned allanite in garnet amphibolites from a paleo-subduction zone: Catalina Schist, southern California. *American Mineralogist* **76**, 589–601.

Spear, F. S. & Pyle, J. M. (2002). Apatite, monazite, and xenotime in metamorphic rocks. In: Kohn, M. J., Rakovan, J. & Hughes, J. M. (eds) *Phosphates—Geochemical, Geobiological and Materials Importance. Mineralogical Society of America and Geochemical Society, Reviews in Mineralogy and Geochemistry* **48**, 293–335.

Spear, F. S. & Pyle, J. M. (2010). Theoretical modeling of monazite growth in a low-Ca metapelite. *Chemical Geology* **273**, 111–119.

Stacey, J. S. & Kramers, J. D. (1975). Approximation of terrestrial lead isotope evolution by a two-stage model. *Earth and Planetary Science Letters* **26**, 207–221.

Tomkins, H. S. & Pattison, D. R. M. (2007). Accessory phase petrogenesis in relation to major phase assemblages in pelites from the Nelson contact aureole, southern British Columbia. *Journal of Metamorphic Geology* **25**, 401–421.

Vidal, O., Parra, T. & Vieillard, P. (2005). Thermodynamic properties on the Tschermak solid solution in Fe-chlorite: application to natural examples and possible role of oxidation. *American Mineralogist* **90**, 347–358.

Vidal, O., De Andrade, V., Lewin, E., Munoz, M., Parra, T. & Pascarelli, S. (2006). *P–T*–deformation–Fe^{3+}/Fe^{2+} mapping at the thin section scale and comparison with XANES mapping. Application to a garnet-bearing metapelite from Sambagawa metamorphic belt (Japan). *Journal of Metamorphic Geology* **24**, 669–683.

Villa, I. M., Bucher, S., Bousquet, R., Kleinhanns, I. C. & Schmid, S. M. (2014). Dating polygenetic metamorphic assemblages along a transect across the Western Alps. *Journal of Petrology* **55**, 803–830.

Wang, E., Kirby, E., Furlong, K., van Soest, M., Xu, G., Shi, X., Kamp, P. & Hodges, K. (2012). Two-phase growth of high topography in eastern Tibet during the Cenozoic. *Nature Geoscience* **5**, 640–645.

Weller, O. M., St-Onge, M. R., Waters, D. J., Rayner, N., Searle, M. P., Chung, S.-L., Palin, R. M., Lee, Y.-H. & Xu, X. (2013). Quantifying Barrovian metamorphism in the Danba Structural Culmination of eastern Tibet. *Journal of Metamorphic Geology* **31**, 909–935.

Whitney, D. L. & Evans, B. W. (2010). Abbreviations for names of rock-forming minerals. *American Mineralogist* **95**, 185–187.

Wing, A. B., Ferry, J. M. & Harrison, T. M. (2003). Prograde destruction and formation of monazite and allanite during contact and regional metamorphism of pelites: petrology and geochronology. *Contributions to Mineralogy and Petrology* **145**, 228–250.

Worley, B. A. & Wilson, C. J. L. (1996). Deformation partitioning and foliation reactivation during transpessional orogenesis, an example from the Central Longmen Shan, China. *Journal of Structural Geology* **18**, 395–411.

Yan, D., Zhou, M., Wei, G., Gao, J., Liu, S., Xu, P. & Shi, X. (2008). The Pengguan tectonic dome of Longmen Mountains, Sichuan Province: Mesozoic denudation of Neoproterozoic magmatic arc–basin system. *Science in China Series D: Earth Sciences* **51**, 1545–1559.

Yan, D.-P., Zhou, M.-F., Li, S.-B. & Wei, G.-Q. (2011). Structural and geochronological constraints on the Mesozoic–Cenozoic evolution of the Longmen Shan thrust belt, eastern Tibetan Plateau. *Tectonics* **30**, TC6005.

Yang, P. & Pattison, D. (2006). Genesis of monazite and Y zoning in garnet from the Black Hills, South Dakota. *Lithos* **88**, 233–253.

Yang, P. & Rivers, T. (2001). Chromium and manganese zoning in pelitic garnet and kyanite: spiral, overprint, and oscillatory (?) zoning patterns and the role of growth rate. *Journal of Metamorphic Geology* **19**, 455–474.

Yang, P. & Rivers, T. (2003). The origin of Mn and Y annuli in garnet and the thermal dependence of P in garnet and Y in apatite in calc-pelite and pelite, Gagnon terrane, western Labrador. *Geological Materials Research* **4**, 1–35.

Zhou, M.-F., Yan, D.-P., Wang, C.-L., Qi, L. & Kennedy, A. (2006). Subduction-related origin of the 750 Ma Xuelongbao adakitic complex (Sichuan Province, China): implications for the tectonic setting of the giant Neoproterozoic magmatic event in South China. *Earth and Planetary Sciences Letters* **248**, 271–285.